DRAG COEFFICIENT REDUCTION OF A 30° YAW ANGLE CUBE SUBJECTED TO ACTIVE FLOW CONTROL DEVICE BY MEANS OF NUMERICAL INVESTIGATION

JEDEDIAH KONG MENG HOI

This report is submitted
in fulfillment of the requirement for the degree of
Bachelor of Mechanical Engineering (Thermal Fluid)

Faculty of Mechanical Engineering

UNIVERSITI TEKNIKAL MALAYSIA MELAKA

17 MAY 2017

DECLARATION

I declare that this project report entitled "Drag Coefficient Reduction of a 30° yaw Angle Cube Subjected to Active Flow Control Device by Means of Numerical Investigation" is the result of my own work except as cited in the references

Signature : ....

Name : ....

Date : ....

APPROVAL

I hereby declare that I have read this project report and in my opinion this report is sufficient in terms of scope and quality for the award of the degree of Bachelor of Mechanical Engineering (Thermal Fluid).

Signature :. ....

Name of Supervisor : ....

Date : ....

DEDICATION

To my beloved mother and father

ABSTRACT

The concept of three different active flow control devices are applied **to** a 30° yaw cube is numerically studied by using a commercial software known as ANSYS Fluent at a Reynolds Number of $\mathbf{6.7{\times}10^4}$. The percentage of drag reduction on the cube is studied for Moving Surface Boundary Layer Control (MSBC), Synthetic Jet (SJ), and Plasma Actuator (PA). MSBC device is implemented by using two small rotating cylinders located at the windward vertical edges of the cube. SJ device is implemented by setting two small opening of $5mm$ beside the windward edges which act as a second source of velocity inlet. PA actuating force is done by applying two force term to two areas located beside the windward edges. As for SJ device, the simulation is run with maximum actuation speed of $1m/s$, $2m/s$, $3m/s$, and $4m/s$. Simulation for PA device is done with force magnitude of $1mN/$m, $2mN/$m, $3mN/$m, and $4mN/$m. The results obtain shows that MSBC device provide greatest average drag coefficient of 28.84% whereas SJ device recorded the lowest drag coefficient reduction of 6.04%. Plasma actuator, being right behind of MSBC device recorded a value of 26.08% reduction of drag coefficient. The result also shows that as active flow control devices are implemented to the cube, region of high vortices formation (which contribute greatly to pressure drag) is significantly reduced.

ABSTRAK

Konsep tiga peranti kawalan aliran aktif yang berbeza digunakan untuk 30° kiub mengoleng yang dikaji dengan menggunakan perisian komersial dikenali sebagai ANSYS Fluent pada nombor Reynolds $\mathbf{6.7 \times 10^4}$*. Peratusan pengurangan heretan dikaji untuk Kawalan Sempadan Permukaan Bergerak (MSBC), Jet Sintetik (SJ), dan Plasma Penggerak (PA). Peranti MSBC dilaksanakan dengan menggunakan dua silinder kecil berputar yang terletak di sudut hadapan kiub. Peranti SJ dilaksanakan dengan menetapkan dua pembukaan kecil 5mm di sebelah sedut hadapan kuib (menghala kea rah sisi) yang bertindak sebagai sumber kedua masuk halaju. PA penggerak daya dilakukan dengan menggunakan dua kuasa sementara kepada dua kawasan yang terletak di sebelah pembukaat kecil SJ. Bagi peranti SJ, simulasi dijalankan dengan kelajuan maksimum angin pada 1m/ (s,) 2m/s, 3m/ (s,) dan 4m/s. Simulasi untuk peranti PA dilakukan dengan kekuatan magnitud 1mN / m, 2mN / m, 3Mn / m, dan 4mN / m. Keputusan yang diperoleh menunjukkan peranti MSBC mencatatkan peratusan pengurangan heretan tertinggi sebanyak 28.84% manakala peranti SJ merekodkan peratusan pengurangan heretan terendah sebanyak 6.04%. Penggerak plasma pula, mencatatkan peratusan pengurangan sebanyak 26.08%, hanya 2.76% perbezaan pengurangan heretan dibandingkan dengan peranti MSBC. Hasil kajian juga menunjukkan bahawa dengan mengimplementasikan peranti kawalan aliran pada kiub, kawasan pembentukan vorteks tinggi (yang menyumbang besar kepada drag tekanan) dikurangkan dengan ketara.*

ACKNOWLEDGEMENT

I would like to express my profound appreciation to my supervisor Dr. Cheng See Yuan for his guidance, advice, as well as support provided to me throughout this research. Although there is slight dispute as well as disagreement among us throughout this research, Dr. still manage to provide a clear path and guidance for me. I sincerely appreciate it.

I would also love to express my gratitude to my friends and lecturers that have provided me with solutions and advices at difficult times faced throughout this research. Your presence and help had always been my motivation to preserve.

Not to forgotten, my family members that have been always supporting me in term of financial and mental, I will not be here without your support.

This research was supported by Universiti Teknikal Malaysia Melaka (UTeM). I thank UTeM for the support in terms of resources provided help completion of this research. Faculty of mechanical engineering (FKM) have been a big contribution for the success of this project. Besides providing computer and software through laboratory located in Fasa B, FKM have also provide seminars, lecturers and lab assistant support to ensure this research is successfully completed.

Last but not least, I would also like to thank other unmentioned parties that have provided guidance throughout the research. I really appreciate your help.

TABLE OF CONTENT

LIST OF TABLES

LIST OF FIGURES

LIST OF ABBEREVATIONS

MSBC	Moving Surface Boundary-Layer Control
SJ	Synthetic Jet
PA	Plasma Actuator
CFD	Computational Fluid Dynamics

LIST OF SYMBOL

f	=	Frequency
D_C	=	Diaphragm Diameter
D_0	=	Orifice Diameter
Δ	=	Amplitude
t	=	Time
$\tilde{u}_0(t)$	=	Fluid leaving Orifice Velocity
C_D	=	Drag Coefficient
F_X	=	Drag Force
A_{ref}	=	Reference Area
F_A	=	Force per Unit Span
$f(t)$	=	Wave Form Function

CHAPTER 1

INTRODUCTION

1.1 BACKGROUND

In general, there are only two distinct types of body, which are streamlined body and bluff body. The major property differentiating these bodies are the type of drag force dominating the body. Viscous drag dominates the drag force of a streamlined body whereas pressure drag dominates the drag force of a bluff body. For a given fixed frontal area and velocity flowing through both types of body, a bluff body will produce higher drag force as compared to a streamline body. This results in many researches done to reduce the drag force for a bluff body. As fluid flows across a bluff body, a large flow separation tends to occur and this will lead to the formation of wake region at the leeward side of the body which prevents pressure from recovering. A larger wake will prevent more pressure recovery from recovering and this will lead to greater pressure drag (Srinivas, 2016). Figure 1.1.1 below shows the variation of drag forces that act on a body.

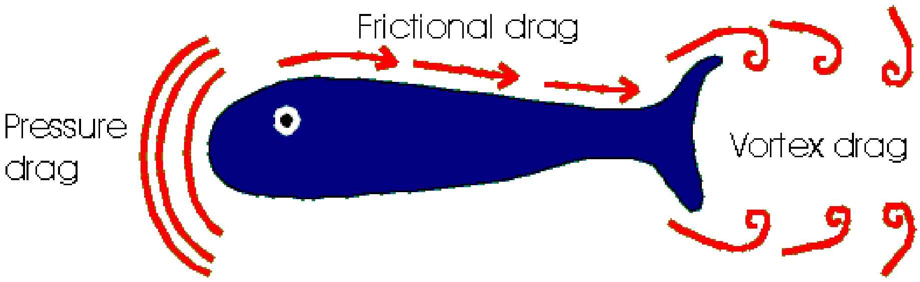

Figure 1.1.1 Variation of Drag Force on a Body (Buchheim J., n.d.)

The modification of wake region is one of the common technique used to reduce the bluff body's drag force. There are two ways to modify the wake region of a body, by using an active flow control device or passive flow control device. Passive control usually utilizes the method of geometry modification and this devices are always operating, regardless of the need. In active flow control method, a device is used to inject extra energy or momentum to the flow. In some cases, active flow control operates only when needed, making it more desirable compared to passive flow control in term of performance. However, additional cost and effort is needed for active flow control. There are three commonly used devices in the application of active flow control which are Synthetic Jet (SJ), Plasma Actuator (PA) and Moving Surface Boundary layer Control (MSBC). These devices have one advantage compared to other device which is it produce zero-net-mass-flux. A research have been done by (Han et. al., 2013) which successfully shown that drag coefficient of a cubical shaped object is reduced with the use of Moving Surface Boundary layer Control (MSBC). On the other hand, a study too have been done by (Pescini et. al., 2016) using plasma actuator to reduce the displacement and momentum thickness of the boundary layer's separated region which in turn reduces the shape factor value.

Although many research have been done independently on using specific active flow control devices, not much attention have been focused on comparing the performance of various flow control devices in drag reduction. This research will be done by using CFD to compare the drag reduction of a 30° yaw cube in a natural flow and various controlled flow techniques.

1.2 PROBLEM STATEMENT

As a flow passes through a cube, the pressure drag dominates the drag force, which means cube is a bluff body. According to a research done by (Xingsi and Siniša, 2013), the use of MSBC technique reduced the drag force of a 30° yawed cube by up to 44%. However, as many research have been done by using individual active flow control device to test the drag reduction of a certain shape, not many research have been done to compare the performance of different active flow control device. In this study, simulation will be done to compare the drag reduction result by using SJ and PA with MSCB on a 30° yawed cube. The positioning for the placement of these two devices will be at the exact same spot at which the MCBS is positioned, which is at the both corners of the windward side of the cube. A fixed angle of 45º actuation from the actuation outlet is implemented for both SJ and PA. The same boundary condition will be used.

1.3 OBJECTIVE

The objectives of this project are:

1) To numerically investigate the effect of active flow control devices on flow of a 30º yaw cube.
2) To quantify the amount of drag coefficient of a cube subjected to constant wind flow and compare the result with the same cube equipped with Moving Surface Boundary-layer Control (MSBC) device, Synthetic Jet (SJ) and Plasma Actuator (PA).

1.4 SCOPE OF PROJECT

The scopes of this project are:

1) Simulating flow around a cube with Reynolds number of 6.7×10^{4}.
2) Using 4 magnitudes of Synthetic Jet maximum actuation speed which are $1\,m/s$, $2\,m/s$, $3\,m/s$ and $4\,m/s$
3) Using 4 magnitudes of Plasma Actuator force value which are $1mN/m$, $2mN/m$, $3mN/m$ and $4mN/m$.
4) Comparing the drag coefficient reduction around a cube after the cube is equipped with MSBC device, Synthetic Jet, and Plasma Actuator.
5) Obtain visualization and compare the flow of air around a 30° yaw cube in natural flow and controlled flow.

CHAPTER 2

LITERATURE REVIEW

2.1 Bluff-Body Aerodynamics

In a research done by Roshko (1993) and Bearman (1997), it have been accurately described that bluff bodies exhibit various major aerodynamic properties such as high pressure drag, large separated flow region, and the existence of vortex shedding. This is caused by the viscous and inviscid flow interaction, which prevent the flow from attaching as it passes through the body. Pressure difference between frontal and leeward faces of the body due to the formation of vortex shedding in the separated region leads to high amount of pressure drag over a long-time average (Sara, 2014). Although vortex shedding is usually associates with two-dimensional body, a research done by Bearman (1977) shows that weaker vortex shedding form may be found in a three-dimensional body. Bearman adds that above some critical Reynolds number, a regular nominal two-dimensional body vortex shedding will display a three dimensional properties through vortex separation, vortex dislocation, looping of vortices, and oblique shedding. As the flow achieves high Reynolds number, numerous three-dimensional motions dominate the wake region. Some of the motions are related to the span wise instabilities of Karman vortices, where others are either related to the smaller-scale to shear layer instability or turbulence flow across the body (Bearman, 1977).

2.2 Cube Flow

In a research done by Ying et. al. (2012), by using Reynolds number of 21400, the aerodynamic patterns of rectangular cylinders with various aspect ratios are determined. From the results obtain, Ying categorized the patterns into three types, namely separated type (B/D=1.0 and B/D=2.0), intermittently reattached type (3.0<B/D<6.0) and fully reattached type (7.0<B/D<10.0). Thus, a cube can be categorize as the same flow as rectangular cylinder with aspect ratio of B/D=2.0. Ying also mentioned that the three-dimensional properties of the flow will become more significant as the location from the separation point is further from the leading point.

From Figure 2.2.1 below, there are recirculating vortices generated around the upper and lower surfaces of the wall, with flow separation at the leading edge remain unattached to the wall. Not only that, the vortex generated behind the cross-section is far away from the back surface, resulting in relatively small Strouhal number.

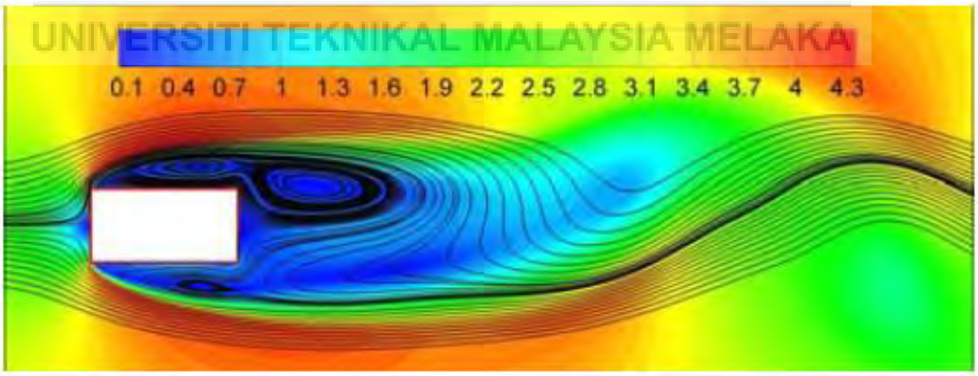

Figure 2.2.1 Instantaneous Velocity Contour with Streamline of B/D=2.0 (Ying et. al., 2012)

In another research done by Xingsi and Siniša (2012) on the flow across a 30º yawed cube, based on the streamline flow diagram, we can deduce that the pressure is maximum at the front left edge of the cube. In Figure 2.2.2, as the flow travel through the cube to the right side of the cube, there is a great pressure drop. This happens as the flow starts separating. The difference in pressure at the front of the cube and the side of the cube causes large drag force.

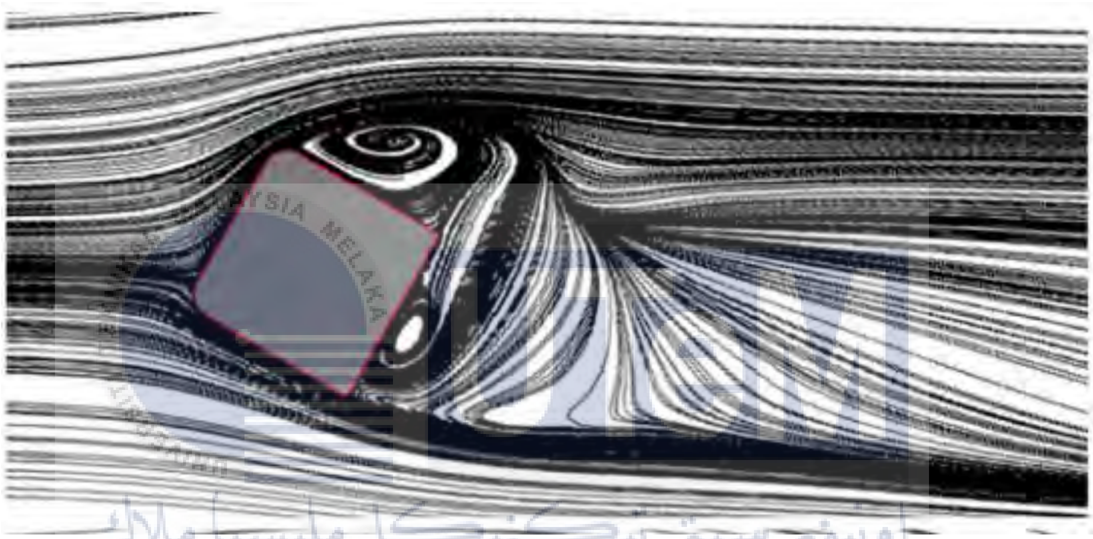

Figure 2.2.2 Streamline of Air Flow across a 30º Yawed Cube (Xingsi and Siniša, 2013)

2.3 Synthetic Jet

Synthetic jet (SJ) is generated by vibrating membrane which is located at the base of an enclosed area. The force generated pushes the air through a circular orifice located at the top of the enclosed area which generates pulsation of air. The SJ actuator is made up of various sections, namely rigid-walled chamber, a round orifice air inlet in the upper surface exposed to outside flow, and an elastic membraned located opposite of the orifice as can be seen in Figure 2.3.1 blow. The working mechanism of SJ actuator have been discussed by Macovei and Florin (2014). Mocevei and Florin (2014) mentioned two major steps in the working mechanism. Firstly, outer air is sucked into the cavity through the orifice when the membrane moves downward. The second step is when the membrane moves upward, causes the fluid to be discharged through the orifice. Vortex ring will be generated as the fluid discharge through the orifice with sufficient energy. Upon continuous upwards and downwards movement of the membrane, generation of vortices column will occur. The vortices column add momentum to the outer fluid without adding mass flux. Mocevei and Florin (2014) also stated that SJ is available for various application due to its wide range of time and length scale.

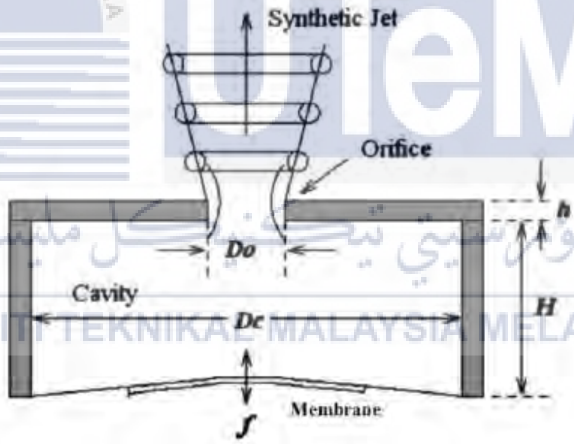

Figure 2.3.1 Schematic Diagram of Synthetic Jet (Macovei and Frunzulica, 2014)

As for the flow separation, it is generally controlled through three working mechanisms. First, additional momentum is injected by the synthetic jet into the ambient freestream flow, adding energy to the retarding boundary layer. Second, high-momentum flow is generated into the boundary layer through continuous successive vortex structures produced by SJ (Zhong et. al., 2007). Third, the detached shear flow or separation bubble becomes unstable due to the oscillation of synthetic jets at frequencies in a specific range. This causes breaking down of the large-scale flow structure correlated with detached shear flow into smaller-scale flow (Tang et. al., 2013)

The periodic motion of diaphragm in the actuator driven by piezoelectric disc produce an unsteady forcing flow (Glezer & Amitay, 2002), which definitely differ from a steady forcing flow. Although this flow is way more complex as compared to a steady forcing flow, it presents three major advantages: smaller order of power requirement magnitude, possible decoupling of actuators from main propulsive system, and SJ are small-sized, light, and autonomous (Greenblatt & Wygnanski 2000).

According to Arun and Ankit (2015), it is expected that maximum jet velocity affects the jet penetration effect. Thus, taking the same average velocity of uniform profile (steady blowing) and parabolic profile (unsteady blowing), a parabolic profile will have the advantage of having higher maximum velocity at the jet centre. In turn, a parabolic profile jet will be able to penetrate deeper as compared to a uniform profile jet. Arun and Ankit (2015) also stated that while there are backflow along the wake centreline during unsteady forcing flow, the effect is negligible. Not only that, Arun and Ankit (2015) discover that upon taking jet momentum into consideration, the drag coefficient is greatly reduced.

A study have been done by Jeon (2004) by implementing periodic blowing and suction from an orifice on a sphere. The Reynolds number used in this study is 10^5 and this study focuses on reducing drag force by the means of using active flow control device. In this study, the fording frequency is set in a range of one to thirty times of the vortex-shedding's natural frequency. The results obtained from this study shows that by the implementation of SJ, drag on the sphere was reduced by 50% by using forcing frequency higher than critical frequency of 2.85U/D (free stream velocity is detonated by U and sphere diameter is detonated by D). As for the forcing frequency value below critical frequency, the drag reduction is not significant as compared to natural case. Additionally, another study had been done by Glezer and Amitay (2002) which shows that drag was reduced greatly by using high forcing frequency from a SJ for the flow across a circular cylinder. In addition, Glezer and Amitay (2002) stated that drag variation was not sensitive to forcing frequency. These results were same to that obtained by Jeon (2004).

Macovi and Frunzulica (2014) mentioned that it is important to choose the suitable amplitude and frequency in order for a clear SJ to be developed. By reviewing the graph located in figure 2 below, the combination of amplitude and frequency should fall in region 4 for SJ to be developed. Based on their study, when applying an amplitude of 0.4mm and frequency of 50Hz, only a weak SJ is developed as shown in Figure below. However, upon applying when an amplitude of 0.8mm and frequency of 400 Hz, it produces much larger amplitude of velocity and in turn, leads to a complete development of SJ.

2.4 Plasma Actuators

Plasma actuators (PA) are device which utilizes electricity to generate wall bounded jet without the use of any moving parts. In the application of controlling air flow, single di-electric barrier discharge actuator is the highly preferred plasma actuator (Vedat, 2016) and is the basis for plasma actuators used (Fridman and Kennedy, 2004). This type of PA have a two unique properties which attracts the attention of researchers, which are it has very short response time and due to its self-limiting property, it is able to sustain large volume discharge at atmospheric pressure without arcing. In a research by Enloe (2004), due to its short time response, this type of actuator has received an exclusive attention of the researchers.

In Figure 2.4.1 below, a PA is made up of two electrodes which are parted by a dielectric barrier material. Slight overlap are given to the electrodes. Upon supplying the electrodes with high voltage a.c. input, ignition of dielectric barrier discharge happens. Image of the ignition can be seen in Figure 2.4.2 (Kozlov, 2007). Typically, ionization begins at the electrode's edge which is exposed to the air at which the intensity of the electric field has its largest value. Upon achieving sufficiently high electric field, electron avalanches and streamer are formed. Streamer are thin ionized channels between electrodes with a lifespan of merely in the order of 10ns.

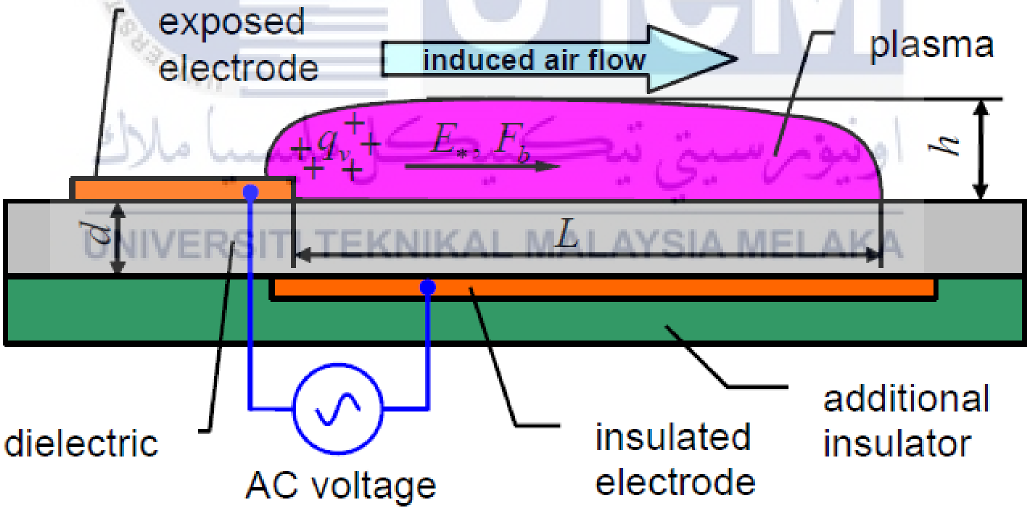

Figure 2.4.1 Schematic Diagram of SDBD Plasma Actuator (Kozlov, 2007)

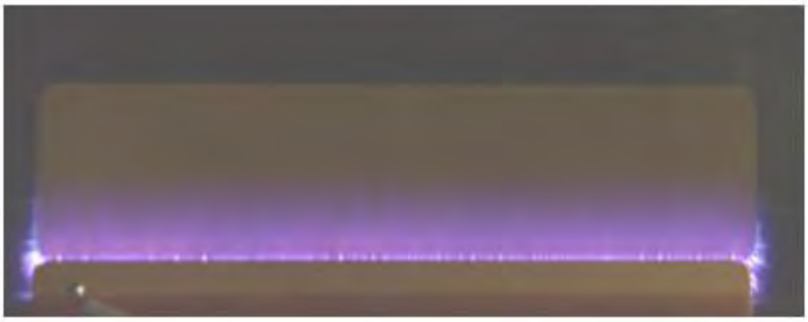

Figure 2.4.2 Top View of Plasma Discharge (Kozlov, 2007)

Streamers begin at the exposed electrode edge and end at the dielectric surface. As it have comparatively high conduction, streamers are able to efficiently transfer electric charges from the exposed electrode to the plasma volume (located nearby dielectric surface). Electric forces are attracted to the dielectric surface and repels from the exposed electrodes due to the same and different charge sign the dielectric surface and exposed electrodes have respectively. After few collisions, momentum are transferred from the charged particles to the non-ionized ambient air. Thus, plasma formation generates momentum to the surrounding fluid (Kozlov, 2007).

The plasma discharge's self-limiting character comes from the build-up of surface charge on the dielectric surface. Thus, in order to prevent the plasma from extinguishing, magnitude of the applied voltage must be continuously increases. As mentioned earlier, plasma formation generates momentum to the surrounding ambient air, and this is the basis flow control method used by a plasma actuator.

There are various advantages of PA in the use of separation control. Firstly, it is a suitable actuator even for flow with Reynolds number with order of 10^6. Secondly, it have great dynamic response as well as low energy input required (voltage applied is large, but with small current drawn). Thirdly, it is inexpensive and very robust (Kozlov, 2007). Fourth, the usage of PA is suitable for both steady and unsteady actuation (with the ability to implement wide range of strategies for unsteady actuations in software). Lastly, effect of PA can be easily included into numerical simulation by adding a simple body force term. This differs from suction or blowing at which local physics of the actuation must be incorporated in the simulations.

Simply by either increasing the applied voltage or optimizing the voltage waveform, the body force per unit volume generated by single di-electric barrier discharge actuator can be increased. However, Kozlov (2007) mentioned that upon increasing the voltage to a certain value, the body force stop increasing with the voltage. In the aspect of voltage waveform, as experimental study done by Enloe et. al. (2004) shows that positive saw tooth waveform produce the best result, in term of maximizing body force.

Unlike synthetic jet, moving parts are not found in a PA and thus, making it less likely to fail. Not only that, due to its small-sized, plasma actuator can simply be placed on surface at which actuation is needed with minimum effort. However, there are a few downside of PA. As mentioned above, high voltage source is needed to sustain the PA. Not only that, as high voltage are required, the exposed electrodes may be dangerous if it comes in contact with any parts of the body. A study by Vernet et. Al. (2013) shows the result of the plasma actuator built burn out after an hour or so of operation, and this shows that good materials are required to make a safe and long lasting PA.

2.5 Moving Surface Boundary-Layer Control

Moving surface boundary-layer control (MSBC) utilizes one of the simplest mechanics among other active flow control device. The MSBC method retard the growth of boundary layer simply by injecting momentum into the existing boundary layer to minimize the relative motion between object surface and free stream fluid. Modi and his colleagues studied of effect on MSBC on various shapes, ranging from two-dimensional air foils (Modi et. al., 1998) to three-dimensional bluff bodies (Modi et. al., 1991). In their study, it can be seen that MSBC effectively reduce the drag force through momentum injection. The method of implementation of MSBC is by the usage of two rotating cylinders. To prevent or delay the flow separation, MSBC utilizes the classical method of moving walls to decrease relative velocity at the flow boundaries.

In another study done by Xingsi and Sinisa (2013), MSBC successfully reduces the drag of a three-dimensional cube subjected to 30º yaw angle. In this study, the comparison of natural and controlled flow shows a difference of 44.1% at which natural flow present a higher drag force. Upon implementing MSBC, the large separation region at the lateral sides of the cube is reduced and this causes the flow to quickly reattach back to the wall surface.

From the iso surface in Figure 2.5.1 and Figure 2.5.2 obtained in their research, four main separated regions are observed. In the first two regions (I and II), it shows the separated regions at the lower and upper surfaces of the cube and the fourth location (IV) is the wake region behind the cube. The separated region III, located around the vertical surfaces of the cube have considerably strong flow separation. This flow separation gradually develop as it flow reaches downstream and thus, contribute greatly to the development of the wake region (IV). However, as the flow is controlled using MSBC, the momentum injected by cylinder 2 causes flow to be nearly attached to the cube surface. This causes flow separation in region III to almost completely disappear and in turn, reduces the wake size (IV). Separated regions I and II are also reduced and become smaller. As the flow separations contribute greatly to the drag, the reduction in flow separation using MSBC greatly reduces the drag of cube. Not only that, by removing flor separation region III, it reduces the pressure drag in this region.

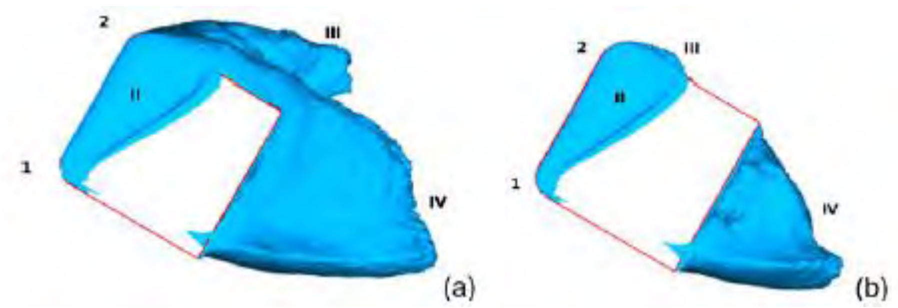

Figure 2.5.1 Iso Surface for Natural Case (a) and Controlled Case (b) in the Case of 30◦ Yaw Angle, Top View (Xingsi and Siniša, 2013)

Figure 2.5.2 Surface for Natural Case (a) and Controlled Case (b) in the Case of 30◦ Yaw angle, Side View (Xingsi and Siniša, 2013)

CHAPTER 3

METHODOLOGY

3.1 Introduction

In this chapter, the methodology used to obtain the drag force is shown. The numerical simulation will be performed using Fluent which can be found in the ANSYS Workbench platform. As this study mainly focuses on numerical simulation, this section will only discuss the steps involved using ANSYS Workbench platform. A flow chart is shown in Figure 3.1.1.

This project begins by geometry drawing which utilizes one of the drawing tool in ANSYS Workbench, Design Modular. After completion of geometry drawing, meshing is done by using ANSYS Meshing. The simulation is run after proper set-up is done in Fluent. After the data is obtained, it is extracted for the purpose of graph plotting and average calculation.

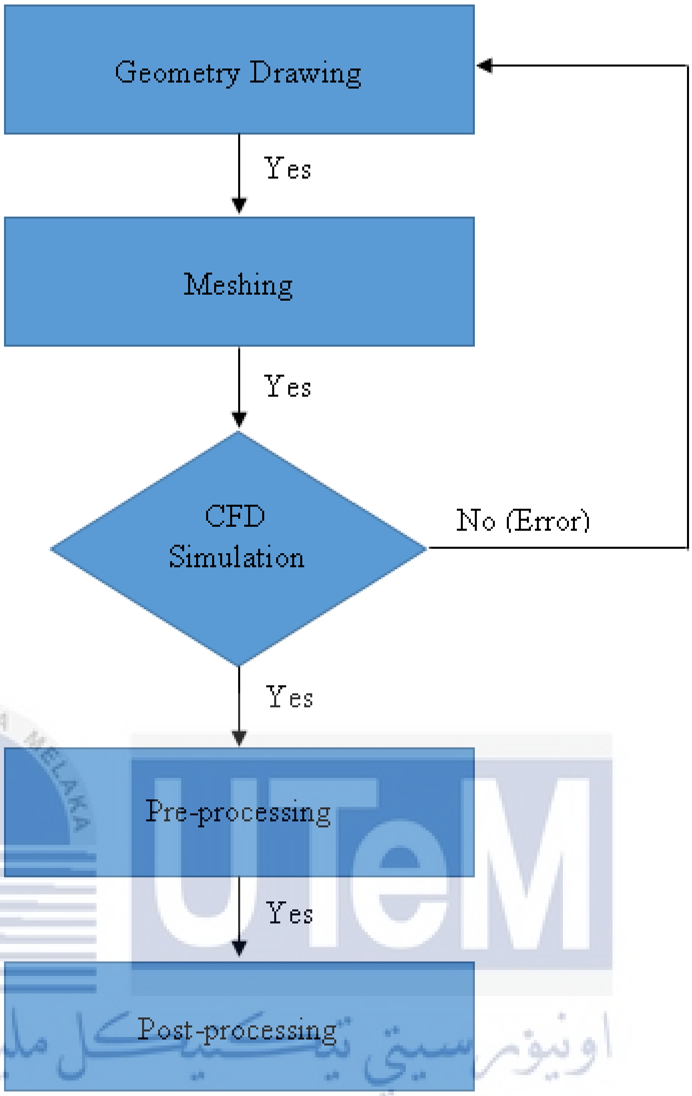

Figure 3.1.1 Flow Chart of CFD Simulation

3.2 Geometry Drawing

By using Design Modular, the geometry as seen in Figure 3.2.1 is drawn.

Figure 3.2.1 Geometry of 30° Yaw Cube

The geometry above consists of 3 rectangular, the innermost is the cube at which airflow will be simulated around it, the middle-sized rectangle is used for meshing purpose, and finally the largest rectangle which is used as a wind tunnel. The orifice diameter for SJ is set to be $D_0 = 5mm$ located right after the curvatures as seen in the red circles in Figure 3.2.2 below. The PA forcing area is also set to be at the same area extending 15mm diagonally at an angle of 45º from the side surface of the cube.

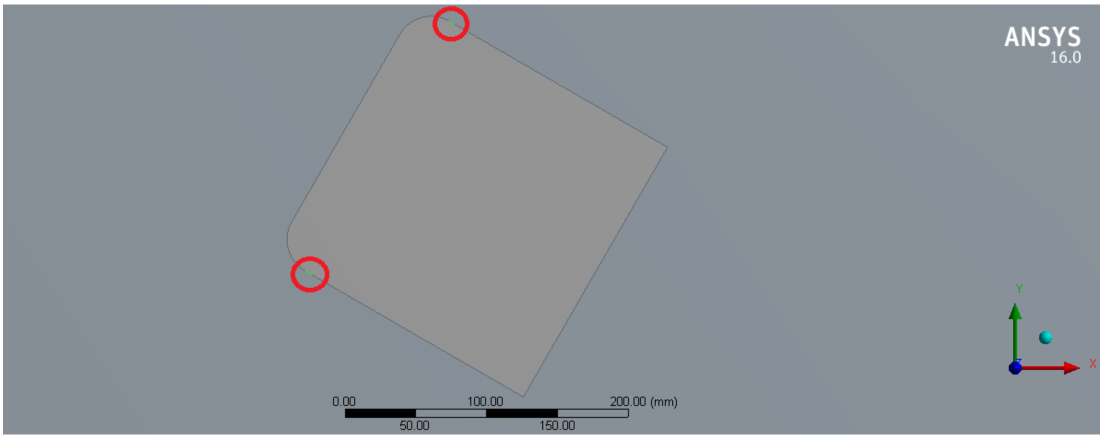

Figure 3.2.2 Location of Synthetic Jet Actuator’s Orifice

The cube has length sides of $W = 203mm$ with rotating cylinders of $D_r = 50.8mm$ at two adjacent vertical surfaces. It is yawed at an angle of 30° and is located $5.5W$ from the inlet and $15.5W$ from the outlet. The cube is placed at the middle of the two separating walls of the numerical wind tunnel which has breadth of $5W$ and length of $21W$.

3.3 Meshing

The meshing elements used for this geometry are made up of quadrilateral and triangle elements. In order to obtain a smoother growth transition, the body of influence sizing is used. The element within the range of body sizing is limited to 20mm. The edge sizing method is applied to the cube's edges with element size of $10mm$ and numerical wind tunnel's edges with element size of $200mm$. The all triangle method is used and a total of 40 inflation layers are applied around the cube, having first layer thickness of $0.1mm$ and growth rate of 1.1. The meshed product is shown in Figure below. The total elements for this mesh is 8162 with minimum orthogonal quality of 0.31076 and maximum skewness of 0.5322.

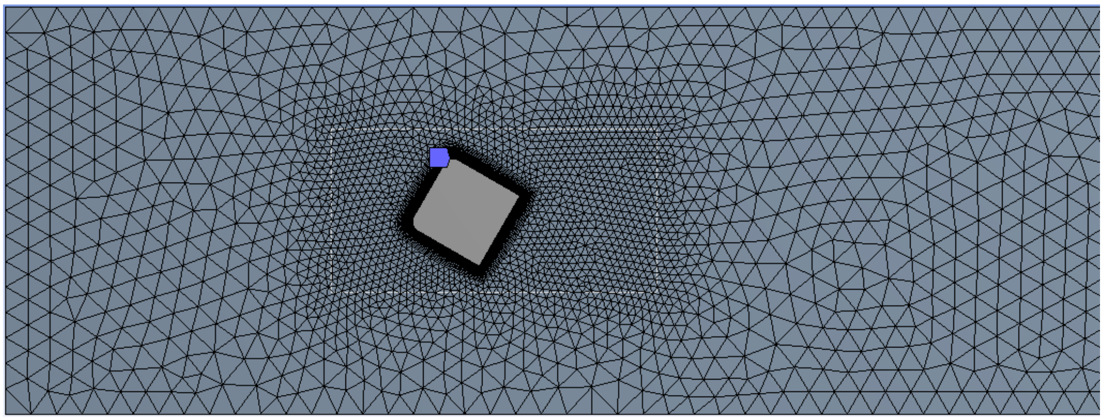

Figure 3.3.1 Meshed Product of Cube

3.4 Pre-processing

All simulations are first run by using PISO method in first order schemes with time step side, $\Delta t = 5e^{-5}$ for a total time, $t = 5e^{-3}$. Following that, the simulations are run in second order schemes until $t^{*} = \Delta t U_0/W \approx 100$ for both the natural and controlled flows. The turbulence model used in this simulation is $k - \omega$ as it works well with separating flow (Andersson et. al., 2012). The fluid property is set to be air in room temperature. (24°C).

A steady and uniform velocity $U_0 = 5\,m/s$ is set at the inlet boundary condition (left-side of the largest rectangle), resulting in $Re = 6.7{\times}10^{4}$ based on the cube's length of $W = 203mm$. Cube's surfaces are subjected to no-slip boundary condition and virtual wind tunnel walls are set to exhibit free-slip property. However, when this simulation is run with the MSBC technique, a tangential velocity of $U_c = 2U_0$ is applied to the rotating cylinder (red region in Figure 3.4.1). The A corner in Figure 3.4.1 below shows the rotating cylinder which will be performing clockwise rotational [with the rotation-axis origin is set at curve's origin (-2.9547e-06, 0.10396)] and the B corner will be rotating in the counter clockwise direction [with the rotation-axis origin is set at the curve's origin (-0.076103, -0.027853)].

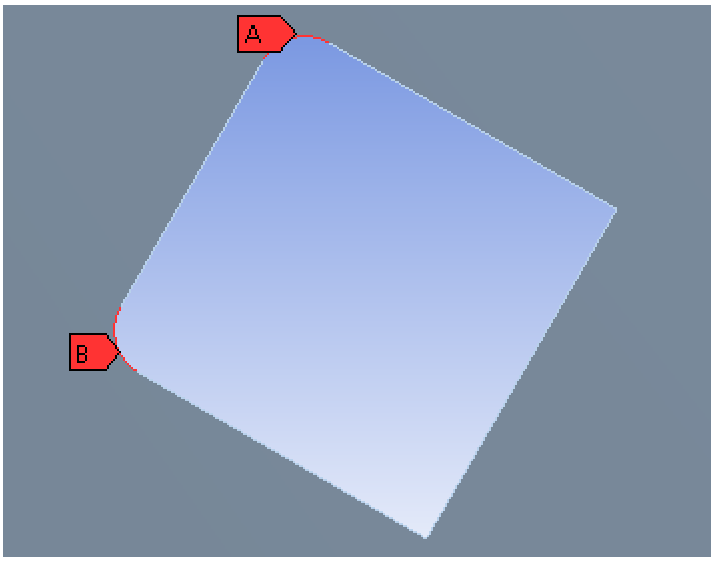

Figure 3.4.1 Location of Rotating Cylinder

In the case of simulating flow by implementing synthetic jet, the flow actuated is not a steady flow. Thus, a new flow command is needed to be defined by using User Defined Function (UDF) function. The UDF compiles the source code written and allows the fluid to flow in according to the written code. According to the study by Macovi and Frunzulica (2014), the flow leaving a SJ actuator's orifice is

$$\widetilde{u_0}(t) = \frac{\pi}{4}.f.(\frac{D_c}{D_0})^2.\cos(2.\pi.f.t) \qquad (1)$$

This equation is the result of differentiating the equation of deformation of plate, followed by applying law of conservation of mass. Upon resolving the equation to x-axis and y-axis (by forcing angle of 45°), the final equation obtained for $4\,m/s$ (maximum air speed actuated) SJ actuator located beside the clockwise cylinder is shown in Figure 3.4.2 (x-axis) and Figure 3.4.3 (y-axis) below. The $4\,m/s$ SJ actuator located right beside the counter-clockwise cylinder is generated by the equation in Figure 3.4.4 (x-axis) and Figure 3.4.5 (y-axis) below.

```
#include "udf.h"
#define DC 0.045
#define DO 0.005
#define FQ 50

DEFINE_PROFILE(cw_x_velocity, ft, var)
{
real flow_time;
face_t f;

flow_time = CURRENT_TIME;

begin_f_loop (f, ft)
{
F_PROFILE (f, ft, var) = 3.863703305*cos(493.8271605*(flow_time));
}
end_f_loop (f,ft)
}
```

Figure 3.4.2 UDF Code for Synthetic Jet Actuator (clockwise side, x-axis)

```
#include "udf.h"
#define DC 0.045
#define DO 0.005
#define FQ 50

DEFINE_PROFILE(cw_x_velocity, ft, var)
{
real flow_time;
face_t f;

flow_time = CURRENT_TIME;

begin_f_loop (f, ft)
{
F_PROFILE (f, ft, var) = 1.03527618*cos(493.8271605*(flow_time));
}
end_f_loop (f,ft)
}
```

Figure 3.4.3 UDF Code for Synthetic Jet Actuator (clockwise side, y-axis)

```
#include "udf.h"
#define DC 0.045
#define DO 0.005
#define FQ 50

DEFINE_PROFILE(cw_x_velocity, ft, var)
{
real flow_time;
face_t f;

flow_time = CURRENT_TIME;

begin_f_loop (f, ft)
{
F_PROFILE (f, ft, var) = 1.03527618*cos(493.8271605*(flow_time));
}
end_f_loop (f,ft)
}
```

Figure 3.4.4 UDF Code for Synthetic Jet Actuator (counter-clockwise side, x-axis)

```
#include "udf.h"
#define DC 0.045
#define DO 0.005
#define FQ 50

DEFINE_PROFILE(cw_x_velocity, ft, var)
{
real flow_time;
face_t f;

flow_time = CURRENT_TIME;

begin_f_loop (f, ft)
{
F_PROFILE (f, ft, var) = -3.863703305*cos(493.8271605*(flow_time));
}
end_f_loop (f,ft)
}
```

Figure 3.4.5 UDF Code for Synthetic Jet Actuator (counter-clockwise side, y-axis)

In the case of plasma actuator, the equations obtained are from two different journals. Equation (2) below shows the simple relation between voltage input, V and force per unit span, F_A with a fixed input frequency of $5kHz$. It is also important to note that the minimum voltage input is $5.31kV$ as mentioned in a journal by West (2012)

$$F_A = 3.26V - 17.32 \tag{2}$$

The following equation (3) shows the wave form function, $f(t)$ obtained from a journal by M. Abdollahzadeh et. al. (2012)

$$f(t) = \begin{cases} 1; & \sin(2\pi ft) \geq 0 \\ -1; & \sin(2\pi ft) < 0 \end{cases} \tag{3}$$

The following equation in Figure 3.4.5(x-axis) and Figure 3.4.6(y-axis) shows the finalized equation for $4mN$/m PA force body area at the region beside the clockwise cylinder whereas the equation for the $4mN$/m PA force body area at the region beside the counter-clockwise cylinder is shows in Figure 3.4.7(x-axis) and Figure 3.4.8(y-axis).

```
#include "udf.h"
DEFINE_SOURCE(source,c,t,dS,eqn)
{
/* Declare Variables */
 real x[ND_ND];
 real flow_time;
 real source, x1, y1;
 /* Call x and y data from FLUENT */
 C_CENTROID(x,c,t);
 flow_time = CURRENT_TIME;
 x1=x[0];
 y1=x[1];
/* Define plasma region. Four inequalities are used to define the rectangular plasma
region. */
/* Apply source term to region inside the four inequalities */
 if ((x1>=0.012697)&&(x1<=0.025687)&&(y1>=0.11845)&&(y1<=0.12595))
 {
 if (sin(31415.93*flow_time>=0))
 {
 source = 3470;
 dS[eqn] = 0;
 }
 else if (sin(31415.93*flow_time<0))
 {
 source = -3470;
 dS[eqn] = 0;
 }
 }
 else
 {
 source = 0;
 dS[eqn] = 0;
 }
 C_UDMI(c,t,0)=source;
 return source;
}
```

Figure 3.4.6 UDF Code for Plasma Actuator (clockwise side, x-axis)

```
#include "udf.h"
DEFINE_SOURCE(source,c,t,dS,eqn)
{
/* Declare Variables */
 real x[ND_ND];
 real flow_time;
 real source, x1, y1;
 /* Call x and y data from FLUENT */
 C_CENTROID(x,c,t);
 flow_time = CURRENT_TIME;
 x1=x[0];
 y1=x[1];
/* Define plasma region. Four inequalities are used to define the rectangular plasma
region. */
/* Apply source term to region inside the four inequalities */
 if ((x1>=0.012697)&&(x1<=0.025687)&&(y1>=0.11845)&&(y1<=0.12595))
 {
 if (sin(31415.93*flow_time>=0))
 {
 source = -2000;
 dS[eqn] = 0;
 }
 else if (sin(31415.93*flow_time<0))
 {
 source = 2000;
 dS[eqn] = 0;
 }
 }
 else
 {
 source = 0;
 dS[eqn] = 0;
 }
 C_UDMI(c,t,0)=source;
 return source;
}
```

Figure 3.4.7 UDF Code for Plasma Actuator (clockwise side, y-axis)

```
#include "udf.h"
DEFINE_SOURCE(source,c,t,dS,eqn)
{
/* Declare Variables */
 real x[ND_ND];
 real flow_time;
 real source, x1, y1;
 /* Call x and y data from FLUENT */
 C_CENTROID(x,c,t);
 flow_time = CURRENT_TIME;
 x1=x[0];
 y1=x[1];
/* Define plasma region. Four inequalities are used to define the rectangular plasma
region. */
/* Apply source term to region inside the four inequalities */
 if ((x1>=-0.088803)&&(x1<=-0.075813)&&(y1>=-0.057350)&&(y1<=-0.049850))
 {
 if (sin(31415.93*flow_time>=0))
 {
 source = 3470;
 dS[eqn] = 0;
 }
 else if (sin(31415.93*flow_time<0))
 {
 source = -3470;
 dS[eqn] = 0;
 }
 }
 else
 {
 source = 0;
 dS[eqn] = 0;
 }
 C_UDMI(c,t,0)=source;
 return source;
}
```

Figure 3.4.8 UDF Code for Plasma Actuator (counter-clockwise side, x-axis)

```
#include "udf.h"
DEFINE_SOURCE(source,c,t,dS,eqn)
{
/* Declare Variables */
 real x[ND_ND];
 real flow_time;
 real source, x1, y1;
 /* Call x and y data from FLUENT */
 C_CENTROID(x,c,t);
 flow_time = CURRENT_TIME;
 x1=x[0];
 y1=x[1];
/* Define plasma region. Four inequalities are used to define the rectangular plasma
region. */
/* Apply source term to region inside the four inequalities */
 if ((x1>=-0.088803)&&(x1<=-0.075813)&&(y1>=-0.057350)&&(y1<=-0.049850))
 {
 if (sin(31415.93*flow_time>=0))
 {
 source = -2000;
 dS[eqn] = 0;
 }
 else if (sin(31415.93*flow_time<0))
 {
 source = 2000;
 dS[eqn] = 0;
 }
 }
 else
 {
 source = 0;
 dS[eqn] = 0;
 }
 C_UDMI(c,t,0)=source;
 return source;
}
```

Figure 3.4.9 UDF Code for Plasma Actuator (counter-clockwise side, y-axis)

The frontal area is set to be $268.01mm$ as well as the length of the cube in reference values. These values will be used during the calculation of drag coefficient, C_D.

$$C_D = \frac{F_X}{0.5\rho U_0^2 A_{ref}} \tag{2}$$

3.4 Post-processing

To provide visualization of the flow, contour diagrams are plotted. The variable that are taken account in this in this visualization is pressure and velocity. This is done for all ten cases of controlled and natural flow. To show the effect of MSBC, the timeframe is selected based on the minimum drag coefficient point achieved after the C_D graph begin showing oscillatory pattern.

CHAPTER 4

RESULTS AND DISCUSSION

4.1 No Flow Control Device

The first case is done by simulating a regular cube, subjected to a constant wind blowing at a speed of 5 m/s. This acts as the base for comparison between other active flow control devices. In the velocity contour diagram which can be seen in Figure 4.1.1 below, there is a large area of low velocity located at the circulated area. This area contributes largest to the pressure drag, similar to what recorded in a research done by Xingsi and Siniša (2013). This area develops a situation where the pressure distribution between the leeward side of the cube and the windward side differs leading to large pressure gradient between the two points which causes pressure drag.

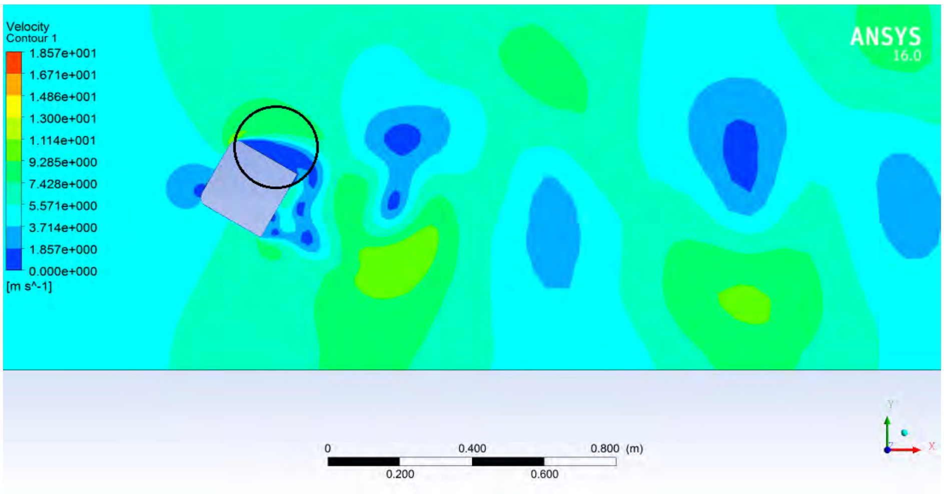

Figure 4.1.1 Diagram of Velocity Contour around a Cube with No Active Flow Control Device

In Figure 4.1.2, it is important to notice the positive pressure at the windward side (high pressure) and the negative pressure at the leeward side (negative pressure) which causes a force pushes the cube backwards (positive x-axis direction). The high-pressure region pushes the cube from the front while the low-pressure region creates a suction zone which sucks the cube backwards.

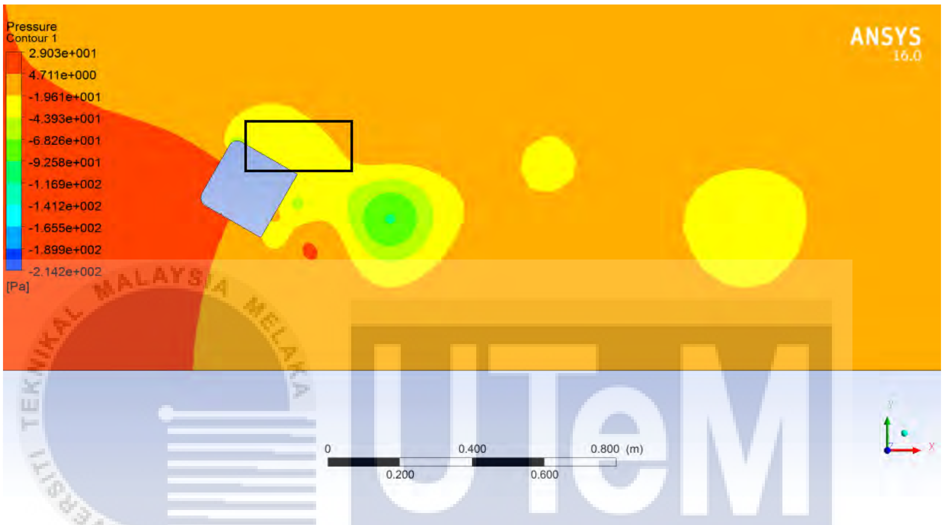

Figure 4.1.2 Diagram of Pressure Contour around a Cube with No Active Flow Control Device

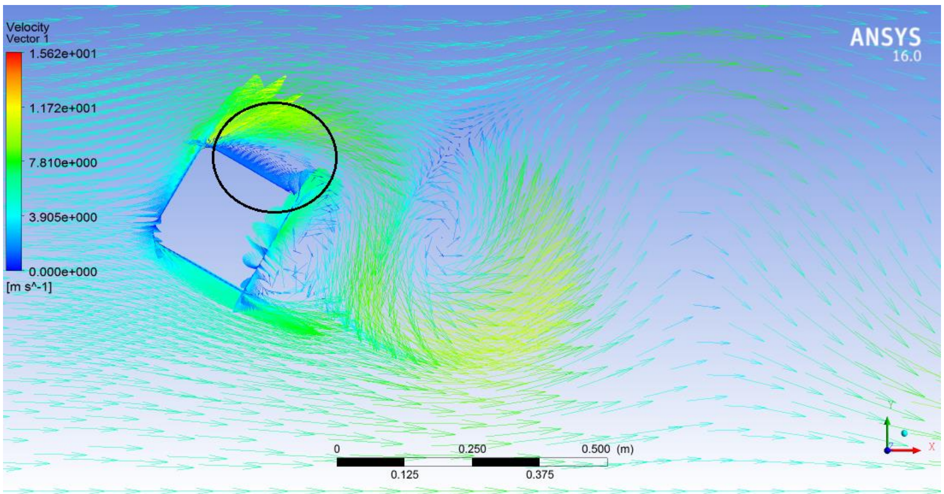

Figure 4.1.3 Diagram of Velocity Vector around a Cube with No Active Flow Control Device

The velocity vector diagram shown in Figure 4.1.3 above displays the backflow region as the flow separates. In the circular area, there are an obvious swirling of flow in it implying there are formation of vortices at that area. Vortex formation is one of the main cause of drop in pressure in a flow.

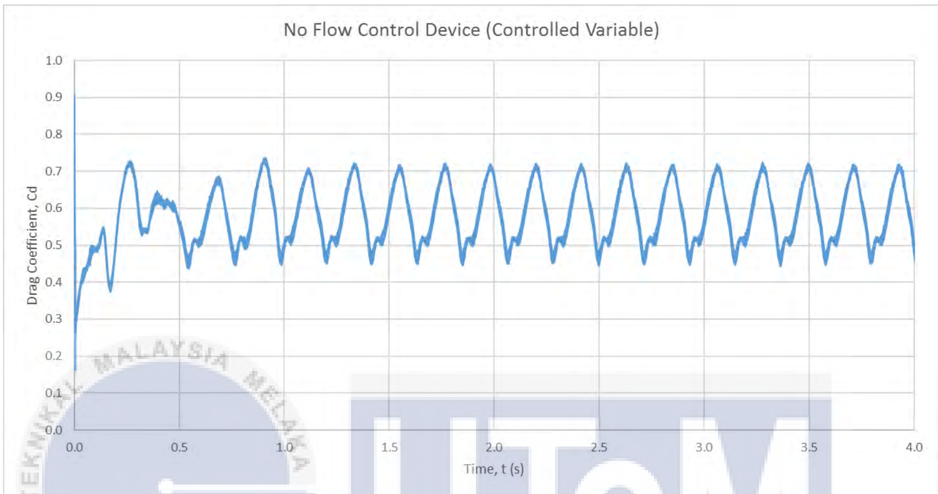

Figure 4.1.4 Graph of Drag Coefficient against Time for Simulation with No Flow Control Device

4.2 MSBC Device

The second case is done by implementing two rotating cylinder to both windward edges of the cube. The speed of the rotating cylinder is $10\, m/s$, which is doubled of the speed of the blowing wind (from the inlet). In Figure 4.2.1, the low velocity region which is present in the previous case (first case) have been significantly reduced. Once again, this is the same results obtained from the study done by Xingsi and Siniša (2013). As the separated flow are being reattached to the cube's wall by the rotating cylinder, the area of low-velocity reduces as well. This in turn reduces the low-pressure region as seen in Figure 4.2.2. The total drag coefficient reduction is 28.84% after implementing MSBC device.

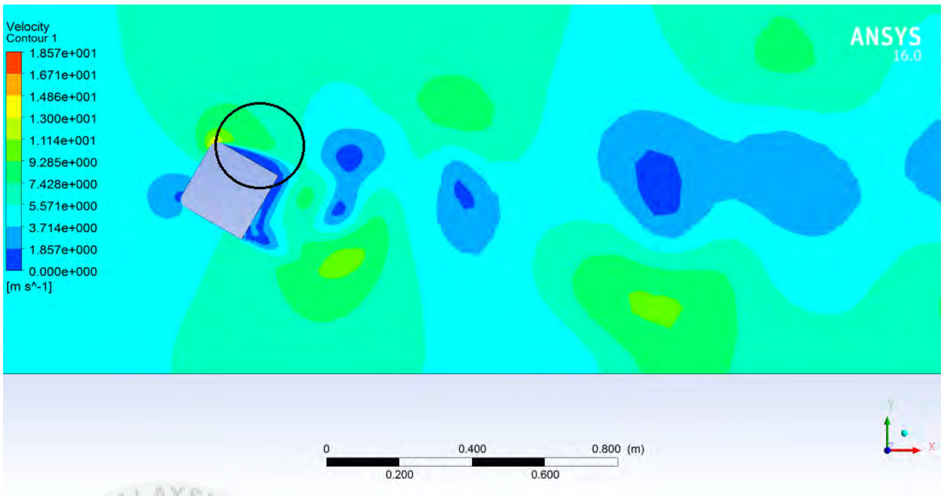

Figure 4.2.1 Diagram of Velocity Contour around a Cube subjected to MSBC Device

From Figure 4.2.2, it is also noticeable that the high-pressure region dominates the flow in the wind tunnel. However, the flow close to the cube are not affected by this phenomenon. As compared to the flow in the first case, the flow in the second case have smaller negative-pressure region nearby the cube which is one of the major source of pressure drag. The area in the black cube in Figure 4.1.2 decreases as MSBC device is used in Figure 4.2.2.

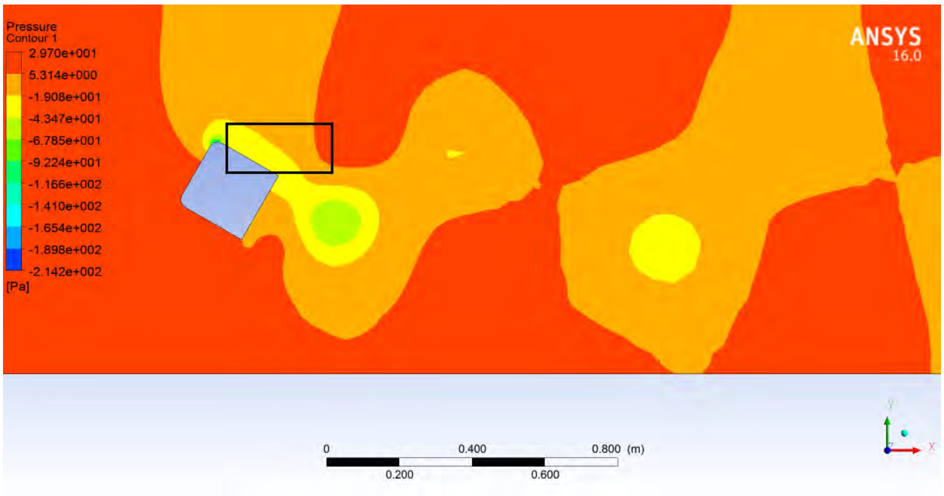

Figure 4.2.2 Diagram of Pressure Contour around a Cube subjected to MSBC Device

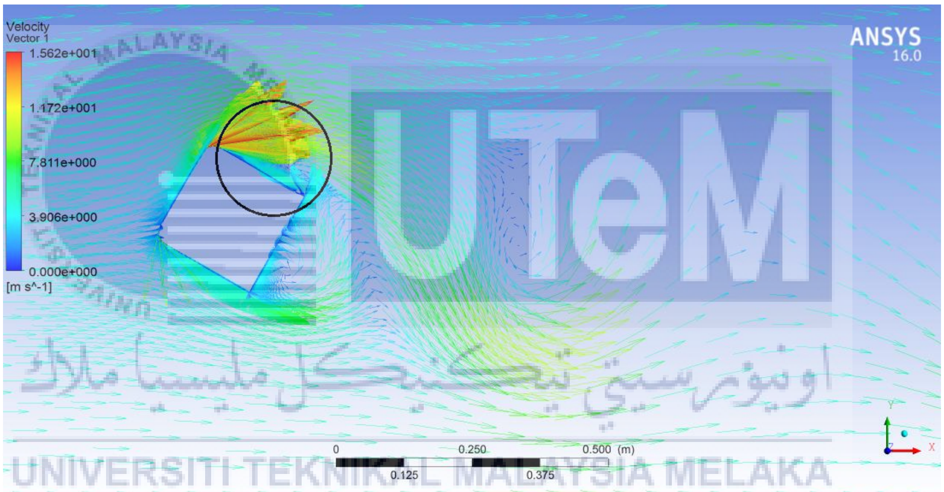

Figure 4.2.3 Diagram of Velocity Vector around a Cube subjected to MSBC Device

The velocity vector diagram for cube subjected to MSBC device shows promising result as expected. The region which used to have formation of vortices were eliminated almost completely as seen in Figure 4.2.3. It is also noticeable that the circulated region display slightly higher air velocity speed compared to the first simulation done.

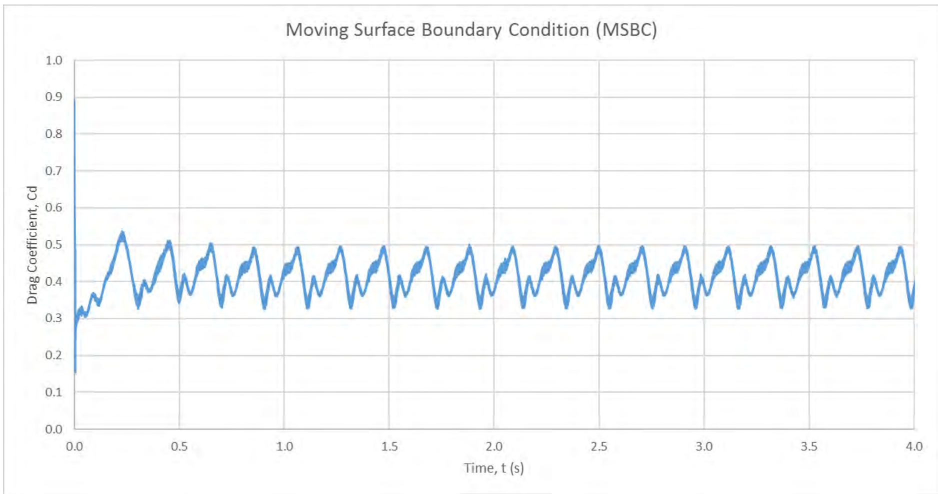

Figure 4.2.4 Graph of Drag Coefficient against Time for Simulation with MSBC Device Implemented on a Cube

4.3 Synthetic Jet

The next few simulations are done by implementing SJ with maximum actuating speed of $1m/s$, $2m/s$, $3m/s$, and $4m/s$ (since SJ is actuated based on a sine graph, the velocity is constantly changing in one oscillation). However, only the visualization of SJ which displays highest drag coefficient reduction will be displayed and discussed here. In this case, it is the SJ with maximum actuation speed of $4m/s$ with a total reduction of 6.04%. If we compare the velocity contour of Figure 4.1.1 (no flow control device) and Figure 4.3.1 (cube subjected to SJ), we can hardly notice the difference of separation region size. This shows that SJ barely alter the flow around the cube.

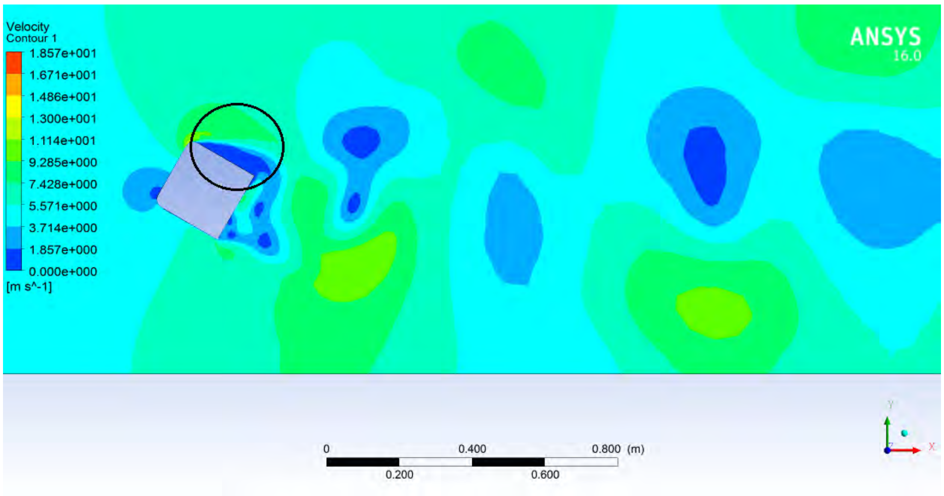

Figure 4.3.1 Diagram of Velocity Contour around a Cube subjected to SJ

Following up, as we compare the pressure contour of the three-different simulation, SJ device shows the lowest windward pressure of the cube but also shows lower leeward pressure. This may slightly disrupt the pressure gradient on the windward and leeward side of the cube but doesn’t reduce the pressure gradient greatly as compared to MSBC device.

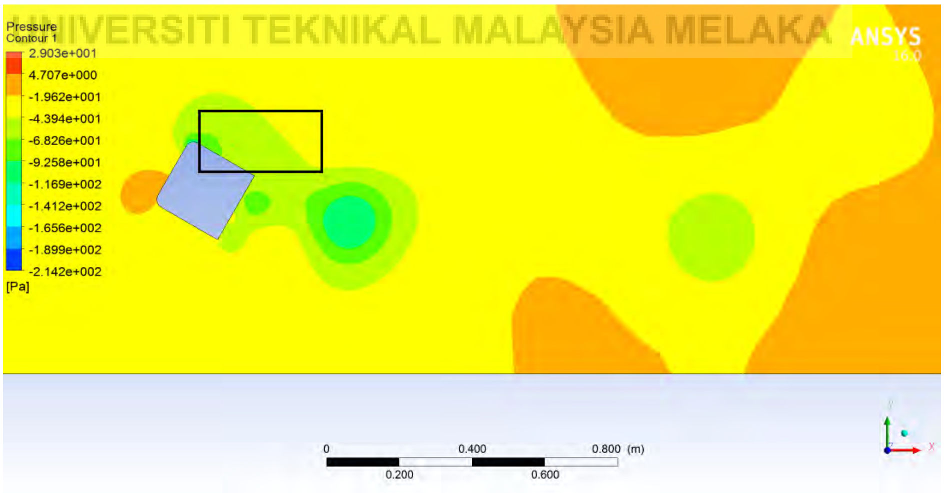

Figure 4.3.2 Diagram of Pressure Contour around a Cube subjected to SJ

The velocity vector for cube subjected to SJ display similar pattern as simulation with no active flow control device. This is expected as the drag coefficient reduction is only by 6.04%.

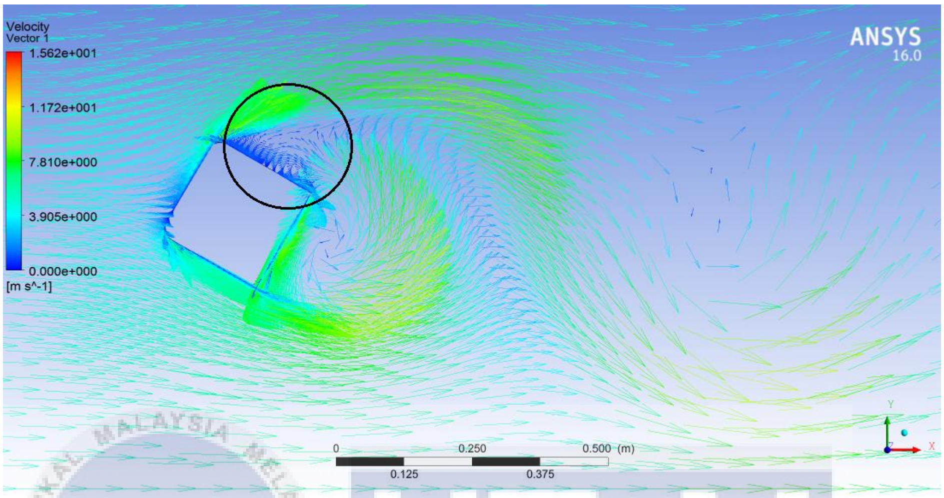

Figure 4.3.3 Diagram of Velocity Vector around a Cube subjected to SJ

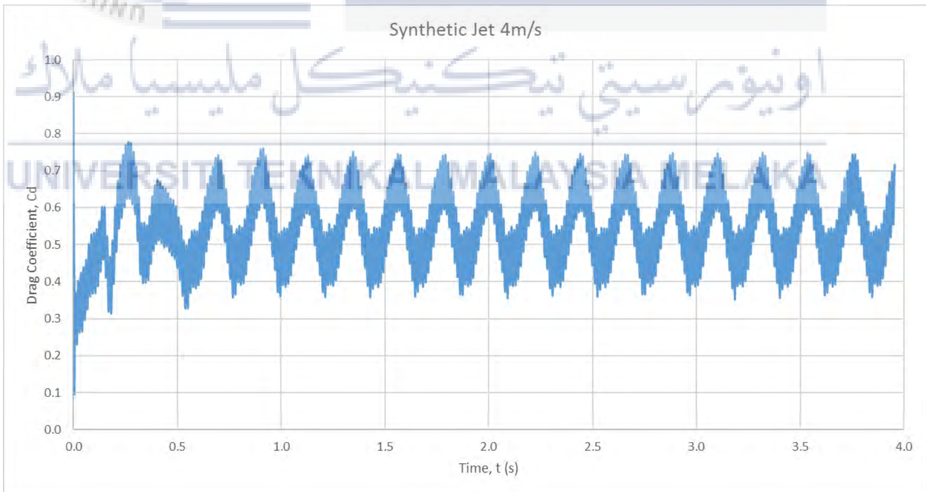

Figure 4.3.4 Graph of Drag Coefficient against Time for Simulation with SJ Device Implemented on a Cube

4.4 Plasma Actuator

The next few simulations are done by implementing force term to two areas around the cube (refer to section 3.2 and UDF code in Figure 3.4.5, Figure 3.4.6, Figure 3.4.7, Figure 3.4.8) of $1mN/$m, $2mN/$m, $3mN/$m, and $4mN/$m. Similar to the discussion done in section 4.3, we will only display and discuss the PA simulation with largest average drag coefficient reduction. PA with force of $4mN/$m recorded the highest percentage reduction of 26.08%. As seen in Figure 4.4.1, the low velocity region diminishes almost completely comparing to the other simulations done previously. In other words, PA successfully achieve the minimum drag coefficient obtained but not the lowest average velocity. At this point, the drag coefficient reaches to the value of 0.209. However, if we compare the graph of PA with other simulation done, the fluctuation of drag coefficient caused by PA is very large. The difference in the highest drag coefficient and lowest drag coefficient value is approximately 0.5. If further research can be done to figure out a way to reduce the maximum drag coefficient, the average drag coefficient by implementing PA device will reduce tremendously.

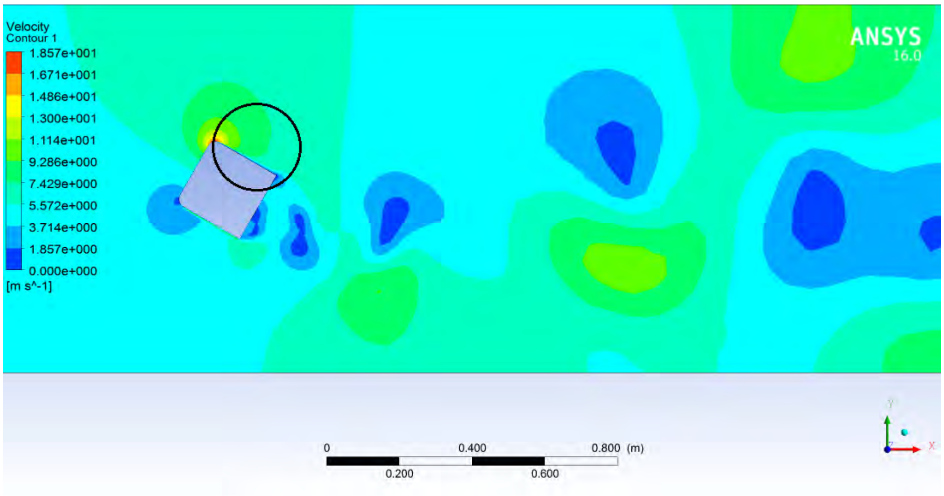

Figure 4.4.1 Diagram of Velocity Contour around a Cube subjected to PA

The pressure contour can be seen in Figure 4.4.2 where the negative low-pressure region diminishes almost completely in the area inside the black rectangular line. This greatly reduce the pressure drag caused by the suction zone.

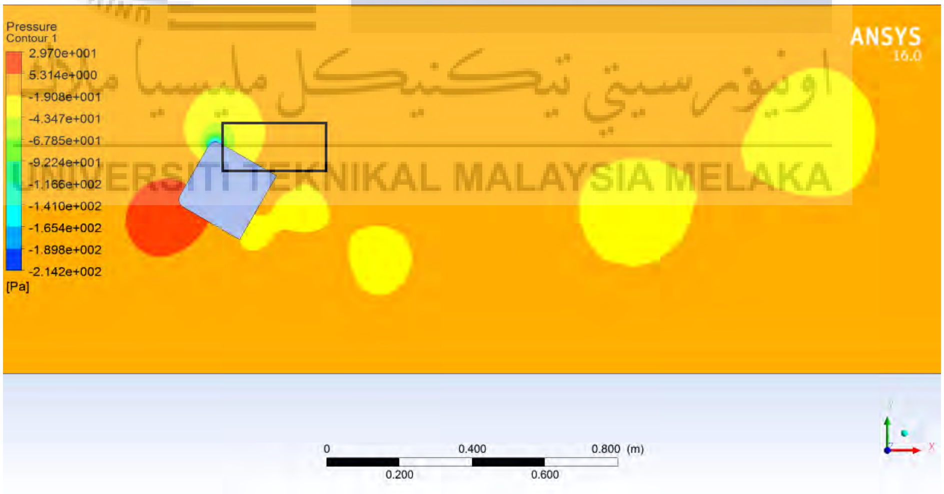

Figure 4.4.2 Diagram of Pressure Contour around a Cube subjected to PA

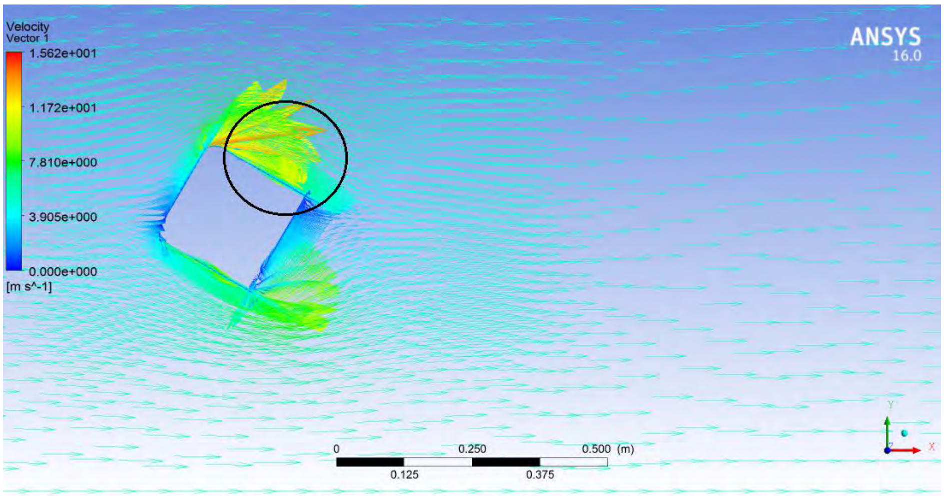

Figure 4.4.3 Diagram of Velocity Vector around a Cube subjected to PA

Velocity vector diagram for cube subjected to PA device shows the most promising result. Putting aside the total removal of vortices in circular region, the wind velocity reading displays the highest value compared to all the other simulation done. This diagram also successfully proves the concept of how the suction zone affects the pressure drag of the cube greatly. As the low-pressure region is removed, the drag coefficient is significantly reduced.

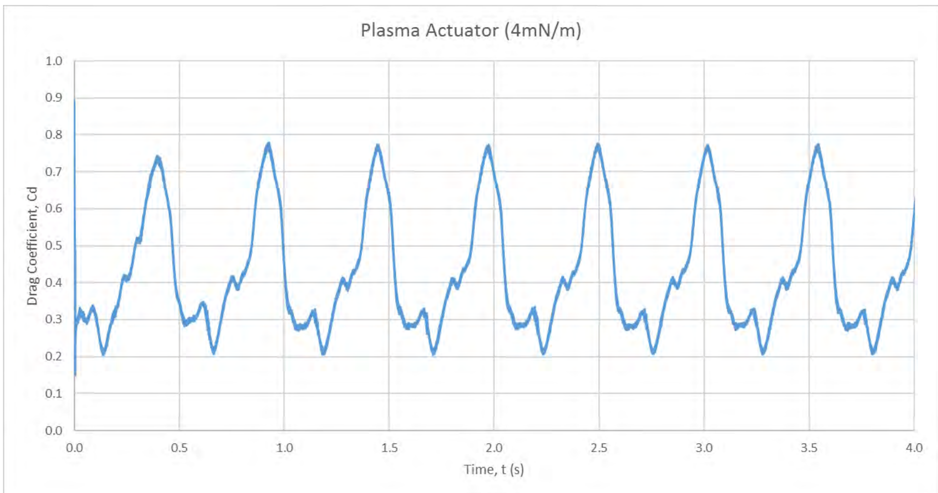

Figure 4.4.4 Graph of Drag Coefficient against Time for Simulation with PA Device Implemented on a Cube

4.5 Grid Independent Test

In order to ensure there are no error associate with the grid size, the final test is done by decreasing the grid size. The original setup for edge sizing and body of influence are further reduced by dividing the value by two (edge sizing for cube wall is reduced from $10mm$ to $5mm$, edge sizing for wind tunnel wall is reduced from $200mm$ to $100mm$, and body sizing is reduced from $20mm$ to $10mm$). As expected, the simulation time increases as the grid size decreases since more calculations are required per volume of grid. The grid independence test is only simulated to the case at which no active flow control is applied (since the grid structure as well as object design is the same for all other cases, testing for only one of the case will do the job). The drag coefficient obtained from this simulation is 0.581 which is only 0.35% difference in value compared to first simulation done (simulation with no active flow control device).

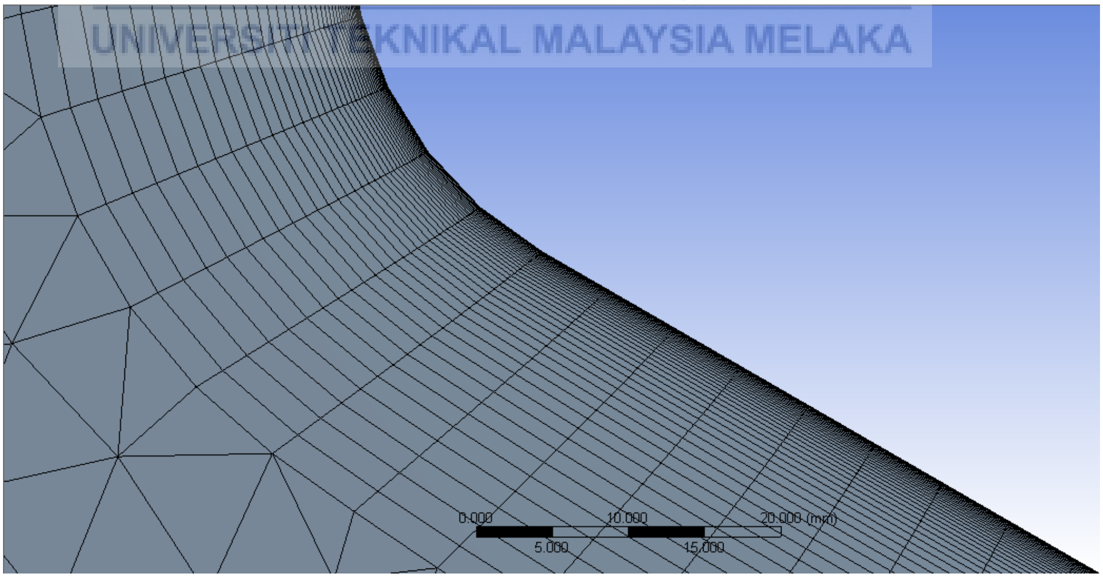

Figure 4.5.1 Scale of 1.5 cm : 20 mm View for Mesh Generated Around a Cube Used for Grid Independence Test

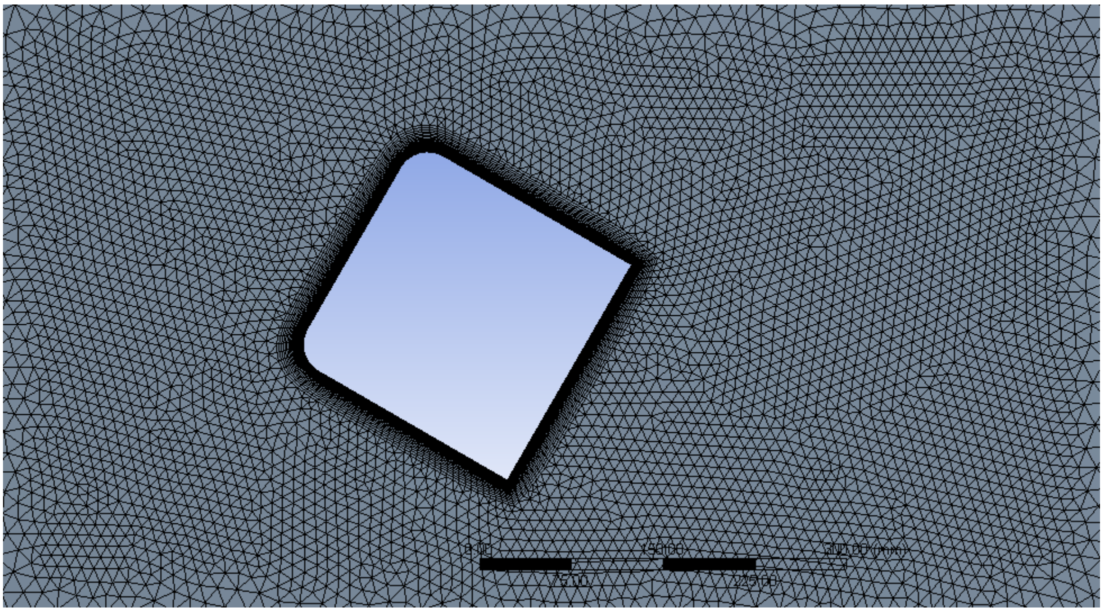

Figure 4.5.2 Scale of 1.5 cm : 75 mm View for Mesh Generated Around a Cube Used for Grid Independence Test

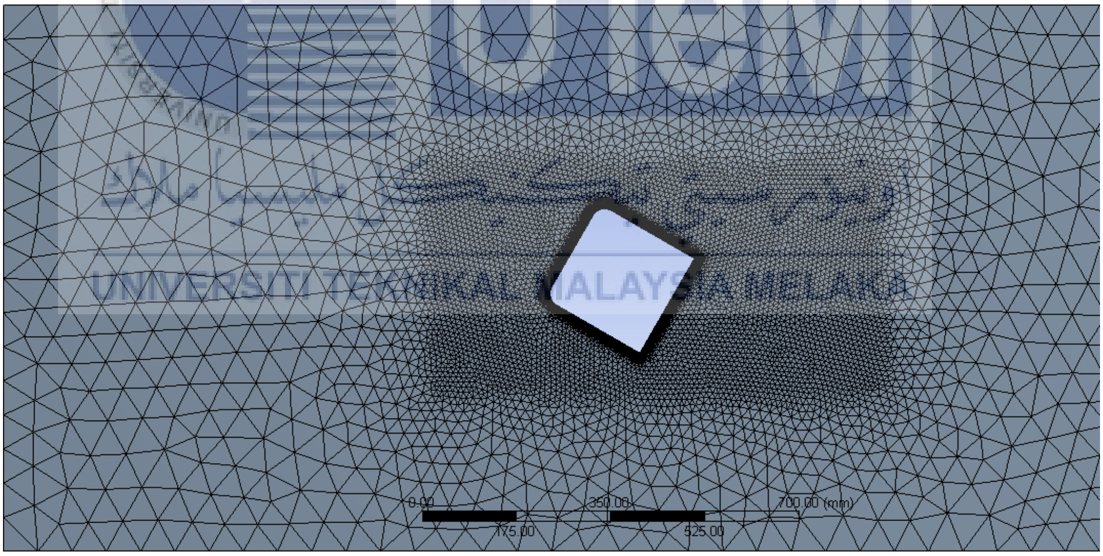

Figure 4.5.3 Scale of 1.5 cm : 175 mm View for Mesh Generated Around a Cube Used for Grid Independence Test

Table 4.5 Details of Meshes used for Grid Independence Test

	Regular Mesh (Used for Simulation of All Cases)	Grid Independence Test Mesh
Inflation First Layer Thickness	$0.1\ mm$	$0.05mm$
Maximum Inflation Layers	40	40
Body Sizing	$20\ mm$	$10\ mm$
Edge Sizing (Numerical Wind Tunnel Outer Domain)	$200\ mm$	$100\ mm$
Edge Sizing (Cube Wall)	$10\ mm$	$5\ mm$
Total Elements	8162	17802
Total Nodes	5845	12182
Drag Coefficient	0.579	0.581
Percentage Reduction	-	0.35

4.6 Data and Comparison

The complete average drag coefficient value as well as the percentage reduction is tabulated in Table 4.5 below. From this table, we can deduce that by increasing the body force of PA device, the average drag coefficient will reduce. However, this concept doesn't apply to the cause of SJ device. Apparently, the SJ with maximum actuation speed of $1\,m/s$ shows greater reduction of average drag coefficient compared to SJ with $2\,m/s$ maximum actuation speed. However, the drag coefficient decreases steadily as the SJ maximum actuation speed is increased to $3\,m/s$ and $4m/s$. Further research need to be done to get a better understanding on the relation between increasing maximum actuation speed on the drag reduction percentage.

Table 4.6 Data of Drag Coefficient and Percentage Reduction

Case	**Average Drag Coefficient, C_d**	**Percentage Reduction, %**
No Flow Control Device (Controlled Unit)	0.579	-
MSBC Device	0.412	28.84
Synthetic Jet ($1\,m/s$)	0.566	2.25
Synthetic Jet ($2m/s$)	0.568	1.90
Synthetic Jet ($3\,m/s$)	0.561	3.11
Synthetic Jet ($4\,m/s$)	0.544	6.04
Plasma Actuator ($1mN/\mathrm{m}$)	0.568	1.90
Plasma Actuator ($2mN/\mathrm{m}$)	0.545	5.87
Plasma Actuator ($3mN/\mathrm{m}$)	0.496	14.34
Plasma Actuator ($4mN/\mathrm{m}$)	0.428	26.08
Grid Independent Test	0.581	0.35

The table above clearly displayed that MSBC device shows the greatest drag percentage reduction of 28.84% while PA with $4mN/\mathrm{m}$ force is only 2.76% behind that value. However, as the average drag coefficient value continuously decreases with increasing force, we do not know at what point this relation will go further. Further research should be done to identify this issue. Similar to the SJ device, more simulations should be done with greater increment of maximum actuation speed. It is also important to note an issue regarding MSBC device, SJ and PA.

4.7 Result Validation

To ensure that the result obtained is correctly simulated, the first two cases of this research is to compare with a reliable source. The first case, which is simulated with no active control equipped on a cube shows similar separation zone with a study done by Xingsi and Sinisa. In their study, it is mentioned that there are four separation regions present in the flow around the cube (can be seen in Figure 4.7.1 below). Xingsi and Sinisa highlighted separation in region III affects the wake region greatly as it develops downstream. This is similar to the results obtained from this research, which shows great separation in the circulated region shown in Figure 4.1.1.

As the cube is equipped with MSBC device, separation region III greatly reduces, which in turn reduce the overall wake region of the flow. Although similar pattern is seen in our visualization with Xingsi and Sinisa's research, the drag coefficient value differs. In the research done by Xingsi and Sinisa's, the average drag coefficient value obtained is 0.635 whereas our study recorded a value of 0.579. This is due to the additional separation region present in a 3-dimensional simulation but not present in a 2-dimensional region. If we observe from Figure 4.7.1 below, separation region I and II falls in the 3rd-dimension region, the z-axis which is not present in this study. As the cube is equipped with MSBC device, Xingsi and Sinisa's study shows a reduction of 46.8% whereas our study only shows a reduction of 28.84%. This may be due to the fact that upon equipping the cube with MSBC device, separation region I and II is slightly reduced.

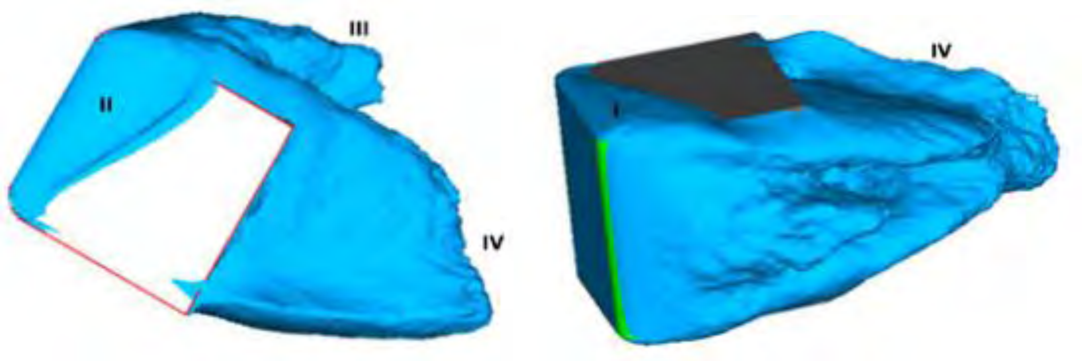

Figure 4.7.1 Iso-surface of the Time-averaged Streamwise Velocity $U = 0$ for No Flow Control Device Case (Xingsi and Siniša, 2013)

4.8 Pressure Fluctuation

Towards the end of this research, an issue was found. In order to ensure that the simulations are simulated in correct manner, the final procedure was to get a glimpse of the whole animation of every simulations in velocity contour as well as pressure coefficient contour. Simulations run by the implementation of synthetic jet on a cube shows great pressure fluctuation which differs from other simulations. Theoretically, the maximum pressure coefficient value that can be achieved in a free flow system is 1.0. However, as a certain flow control device is implemented, this value may increase significantly. In the flow involving synthetic jet ran in this experiment, the pressure coefficient value fluctuates significantly, from a minimum value of -13.4 to a maximum value of 15.7. This questions the reliability of the synthetic jet results. As this is the final stage of the research, there are insufficient time to proceed with more simulations to identify the exact mistake done. Thus, the conclusion drawn from this issue is due to numerical error. The figure below shows the graph of pressure coefficient against time step for synthetic jet (inlet).

As the domain obtained for this simulation is based on an experiment done on MSBC device, a larger domain may be the key to solving this issue. Further research should be done to identify this problem.

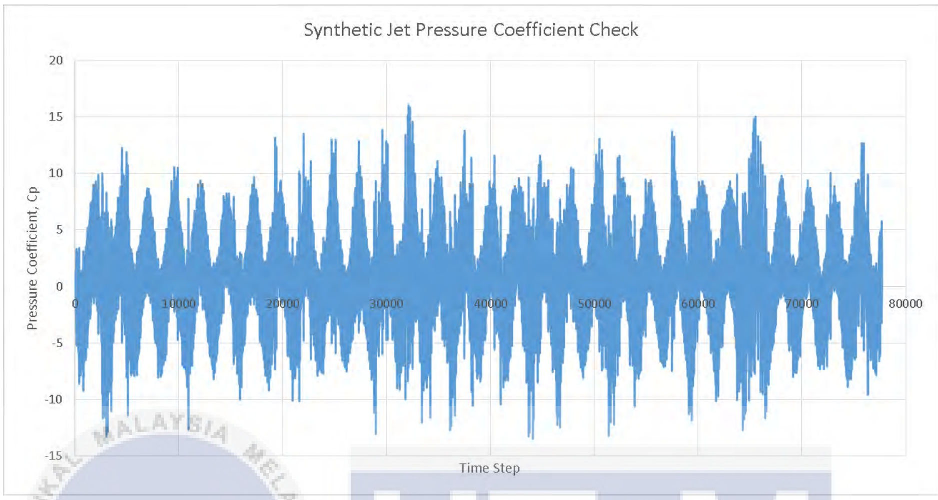

Figure 4.8.1 Graph of Pressure Coefficient against Time Step for Synthetic Jet Implemented on a Cube

CHAPTER 5

SUMMARY

5.1 Conclusion

This study focuses on investigating and comparing the drag coefficient reduction of a 30° yawed cube subjected to various active flow control device. This includes simulating the cube with MSBC, SJ and PA device. Results were obtained from simulation of devices with multiple actuation configuration operating at steady modes.

From the first simulation case (with no active flow control device attached to the cube), we manage to identify the large separation region. As similar setup is simulated with SJ, MSBC and PA device, the large separation area diminishes for MSBC and PA device but not for SJ device. The visualization for SJ device is similar to cube with no flow control device. Thus, the drag coefficient reduction for SJ device is only 6.04% whereas MSBC and PA device shows a reading of 28.84% and 26.08% respectively.

Thus, this research clearly shows that MSBC device has the best drag coefficient reduction property followed by PA device. However, further research need to be done to identify the pressure fluctuation issue faced. As the reliability of SJ device is questionable, it is best not to include the comparison of SJ device in this research.

5.2 Future Research

Due to time limitation and resources available, there's only so much that this research can investigate. However, further research can be done to obtain a more accurate and wider range of variables. For example, this research only covers up to 4 different magnitudes for SJ and PA device. As mentioned earlier, by increasing the magnitude of SJ and PA device, greater drag coefficient reduction is obtained. Thus, future research may be done with larger magnitude range. However, more research also need to be done to accurately determine the optimum maximum voltage that should be used in operating the PA device as well as the maximum frequency for operating the SJ device.

More research should be done to determine the fluctuating issue faced during simulation done by SJ device, possibly simulating the setup with a larger domain area of reducing the maximum actuating speed.

The number of dimensions a simulation is done also should be considered. As compared earlier to the research done by Xingsi and Sinisa, a 3-dimensional object exhibit properties that a 2-dimensional object doesn't. Though 3-dimensional simulation may not be possible for this research, we believe that it is possible for a masters or doctorate research with sufficient time and funds. However, to properly identify the suitable magnitude and direction for body force (for PA) and actuation (for SJ) may be tough in a 3-dimensional manner.

Instead of only simulating the research regarding this manner. I believe that future research should be done on an actual model to ensure that simulations exhibit similar properties as experimental research. It is hope that this study will be beneficial for future work, which acts as a base for research regarding active flow control device.

REFERENCES

Andersson, B., Andersson, R., Hakansson, L., Mortensen, M., Rahman, S., Berend. V. W., (2012). Computational Fluid Dynamics for Engineers, Cambridge University: Cambridge University Press.

Arun, K.S., and Ankit, S., (2014). Suppression of vortex shedding around a square cylinder using blowing. Sadhana, 40 (3), pp. 769-785.

Buchheim, J (n.d.). A Quick Course in Ichthyology. Retrieved from http://www.marinebiology.org/fish.htm

David, M., Jason, V., Micheal, A., Chris, L., Edward, D., Ajith, R., Anna, D., (2012). A Different Approach to the Aerodynamic Performance of Tall Building. CTBUH Journal, 4, pp. 18-23.

Enloe, C. L., McLaughlin, T. E., VanDyken, R. D., Kachner, K.D., Jumper, E. J., Corke, (2004). Mechanisms and Responses of a Single Dielectric Barrier Plasma Actuator: Plasma Morphology. AIAA Journal, 42 (3), pp. 589-594.

Fridman, A., and Kennedy, L. A., (2004). Plasma Physics and Engineering, Taylor & Francis, New York.

Glezer, A., Amitay, M., (2002). Synthetic Jets. Annu. Rev. Fluid Mech. 34, pp. 503–529.

Greenblatt, D. and Wygnanski, I., (2000). The Control of Flow Separation by Periodic Excitation. Progress in Aerospace Sciences, 36, pp. 487-545.

Jeon, S., Choi, J., Jeon, W.-P., Choi, H., Park, J., (2004). Active Control of Flow over a Sphere for Drag Reduction at a Subcritical Reynolds Number, J. Fluid Mech, 517, pp. 113–129.

Kozlov, A. V., (2007). Plasma Actuators for Bluff Body Flow Control. Department of Aerospace and Mechanical Engineering. Notre Dame, Indiana.

M. Abdollahzadeh, J. Páscoa, P. Oliveira, (2012). Numerical Modeling of Boundary Layer Control Using Dielectric Barrier Discharge. IV Conferência Nacional em Mecânica dos Fluidos, Termodinâmica e Energia.

Macovei, A. C., (2014). Numerical Simulations of Synthetic Jets in Aerodynamic Applications. Incas Bulletin, 6 (1), pp. 81-93.

Modi, V.J., Fernando, M.S.U.K., Yokomizo, T., (1991). Moving Surface Boundary Layer Control as Applied to Two-Dimensional and Three-Dimensional Bluff Bodies. J. Wind Eng. Ind. Aerodyn. 38, pp. 83–92.

Modi, V.J., Munshi, S.R., Bandyopadhayay, G., Yokomizo, T., (1998). High Performance Airfoil with Moving Surface Boundary-Layer Control. J. Aircr. 35, pp. 544–553.

Romain, F., (2015). Drag Reduction using Plasma Actuators. Licentiate Thesis. KTH Engineering Sciences. Stockholm, Sweden.

Roshko, A., (1993). Perspectives on Bluff Body Aerodynamics. J. Wind Eng. Ind. Aerodyn, 49 (1), pp. 79–100.

Sara, C., (2014). Active Control of the Wake from a Rectangular-Sectioned Body. Department of Aeronautics, Imperial Collage London.

Sohankar, A., (2004). Flow over a Bluff Body from Moderate to High Reynolds Numbers using Large Eddy Simulation. Computers & Fluids 35, pp. 1154-1168.

Tang, H., Pramod, S., Yingying, Z., Jiaxiang, D., Yanhua, W., (2014). On the use of synthetic jet actuator arrays for active flow separation control. Experimental Thermal and Fluid Science, 57, pp. 1-10.

Vedat, O., (2016). Strategies for the Applications of Flow Control Downstream of a Bluff Body. Flow Measurement and Instrumentation, http://dx.doi.org/10.1016/j.flowmeasinst.2016.08.008.

Vernet, J., Örlü, R., Efraimsson, G., Alfredsson, P. H., (2013). Experimental Study of the Electric Wind Induced by a Dielectric Barrier Discharge Plasma. 4th International Conference on Jets, Wakes and Separated Flows (CJWSF2013). 17-21 September, Nogoya, Japan, pp. 1-6.

West, Thomas Kelsey IV, (2012). Numerical investigation of plasma actuator configurations for flow separation control at multiple angles of attack. Master Theses. 5197.

Xingsi, H., Siniša, K., (2013). Large Eddy Simulation of Flow Control around a Cube Subjected to Momentum Injection. Springer Science+Business Media Dordrecht 2013.

Xuyong, Y., Fuyou, X., Zhe, Z., (2012). Numerical Simulation and Visualization of Flow around Rectangular Bodies. The Seventh International Colloquium on Bluff Body Aerodynamics and Applications (BBAA7). 2-6 September. Shanghai, China, pp. 272-281.

Zhong, S., Jabbal, M., Tang, H., Garcillan, L., Guo, F., Wood, N., Warsop, C., (2007). Toward the Design of Synthetic–Jet Actuators for Full-Scale Flight Conditions, Flow, Turbul. Combust. 78, pp. 283–307.

LIST OF APPENDICES

APPENDIX A1 PSM I Grant Chart

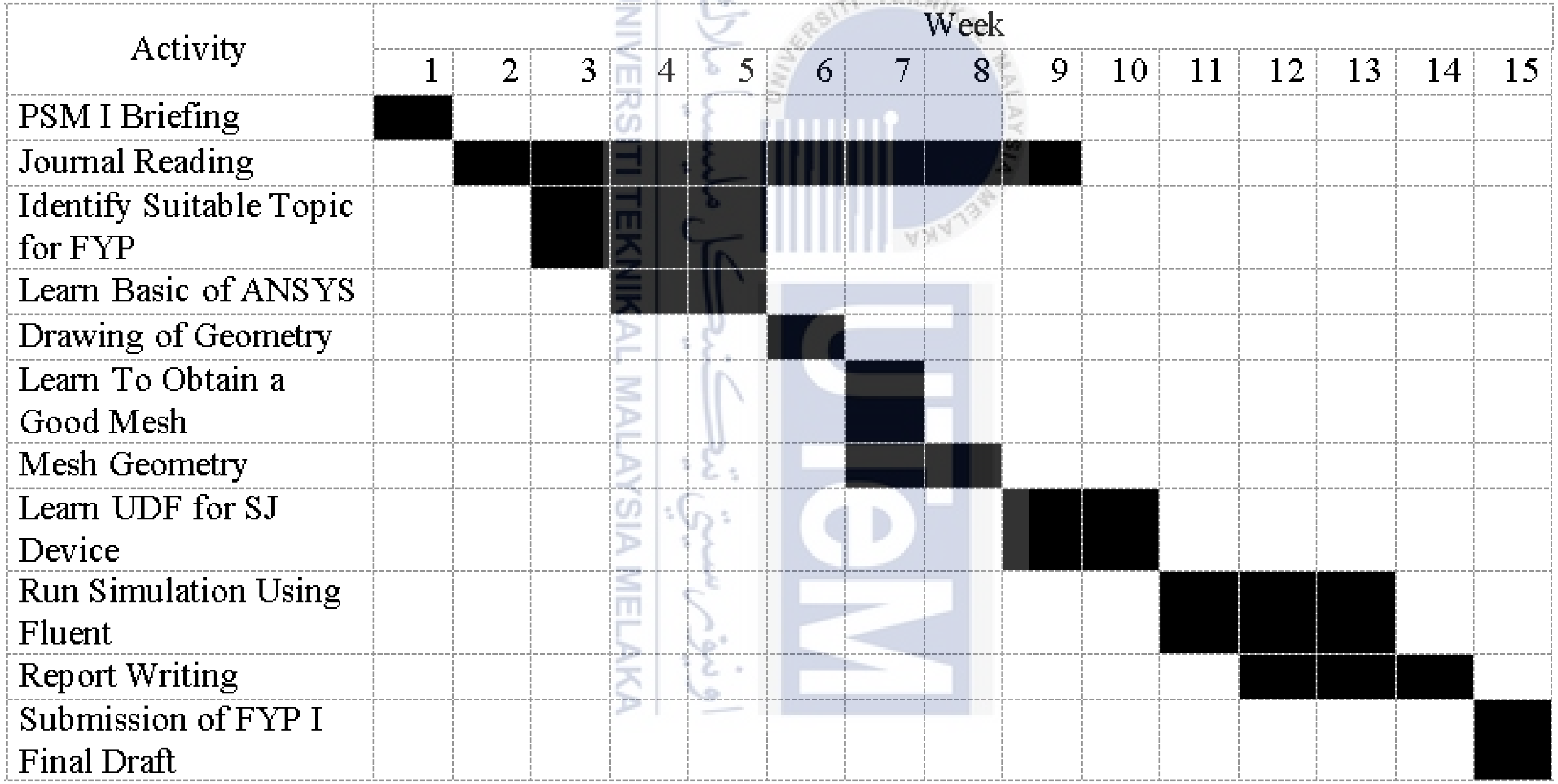

APPENDIX A2 PSM II Grant Chart

Activity	Week 1	2	3	4	5	6	7	8	9	10	11	12	13	14	15
PSM II Briefing	■														
Run Simulation of SJ Implemented of Cube (10m/s)		■													
Identify Error in Results obtained for SJ Simulation			■												
Run Simulation of SJ Implemented on Cube (4m/s, 3m/s, 2m/s, 1m/s)				■	■										
Write Code for PA Body Force						■									
Run Simulation for PA Implemented on Cube (4mN/m)							■								
Run Simulation for PA Implemented on Cube (3mN/m, 2mN/m, 1mN/m)								■	■						
Run Simulation for All Cases to Identify Pressure Fluctuation										■	■	■			
Run Simulation for Grid Independence Test													■		
Report Writing													■	■	■
Submission of FYP II Final Draft															■

APPENDIX B1 Graph of Drag Coefficient against Time for Simulation with SJ Device Implemented on a Cube (1m/s)

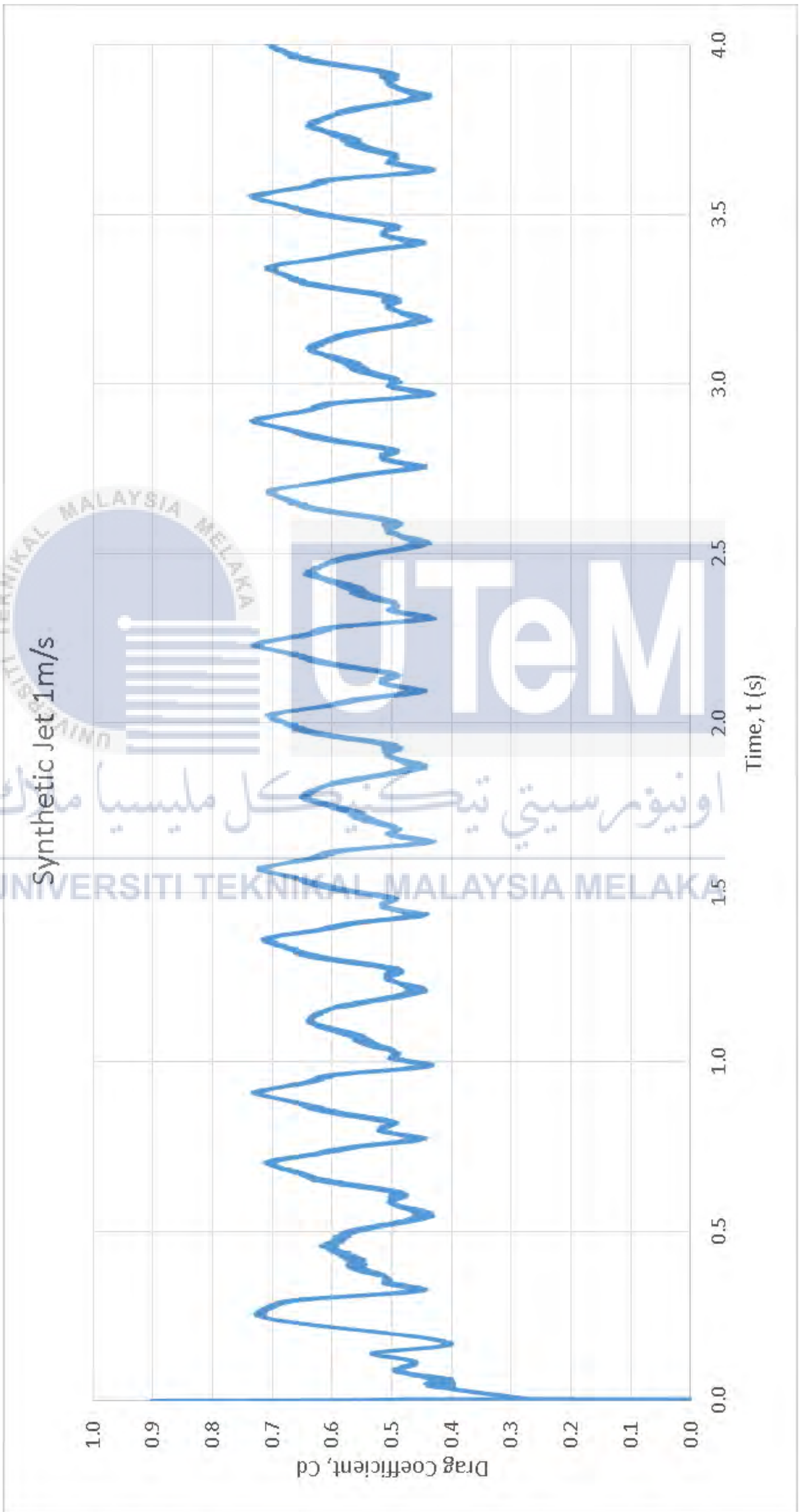

APPENDIX B2 Graph of Drag Coefficient against Time for Simulation with SJ Device Implemented on a Cube (2m/s)

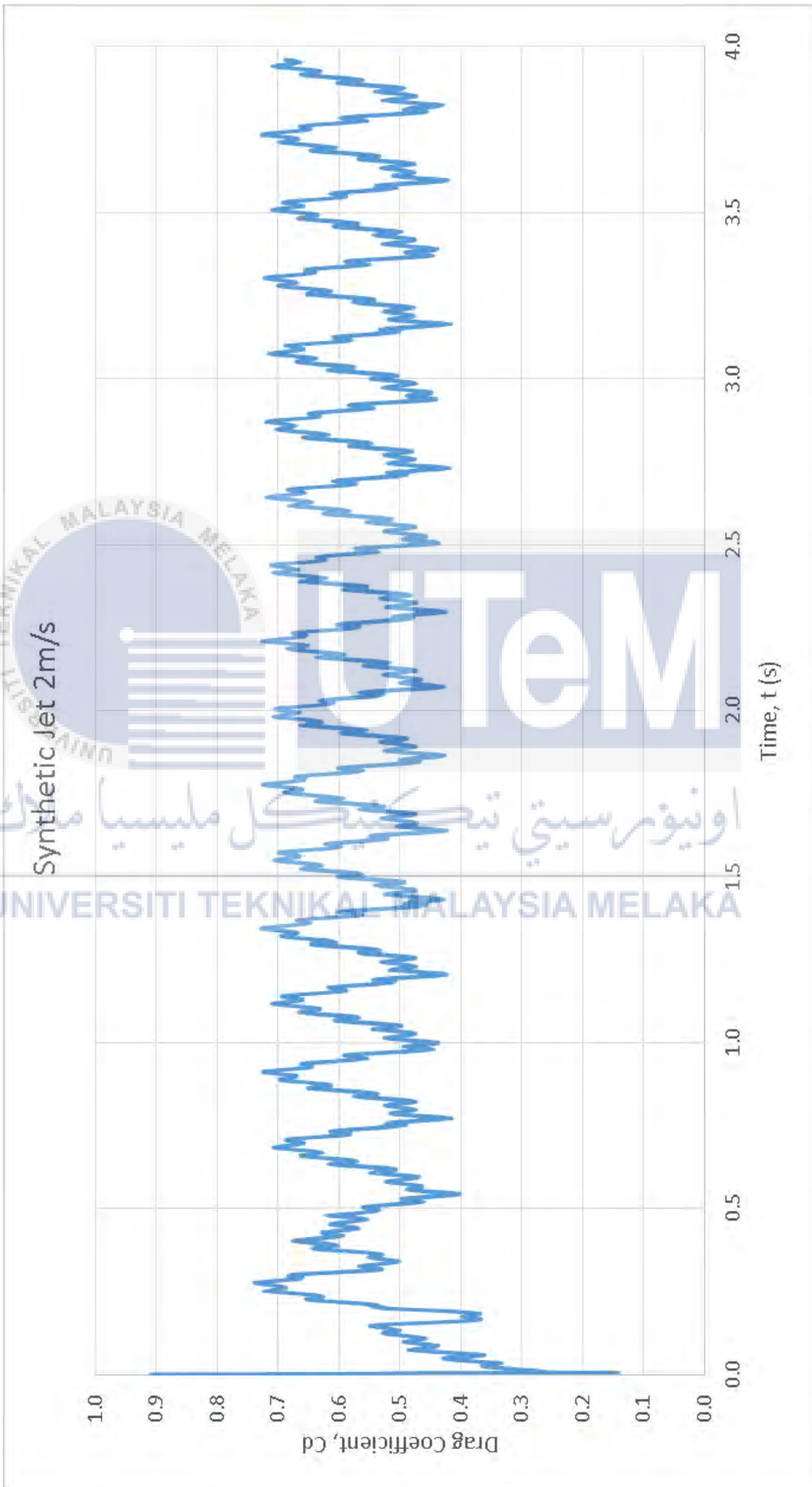

APPENDIX B3 Graph of Drag Coefficient against Time for Simulation with SJ Device Implemented on a Cube (3m/s)

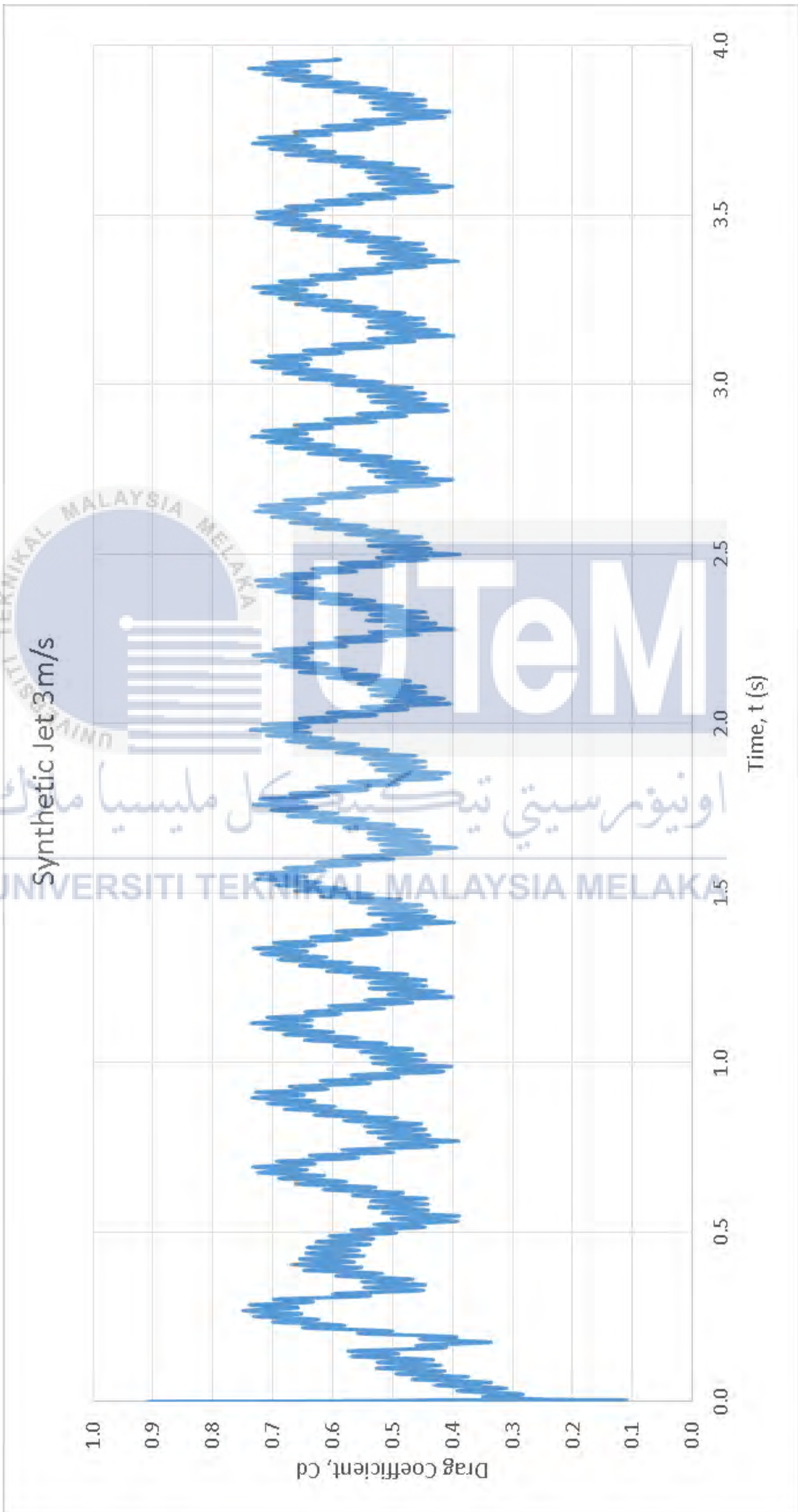

APPENDIX C1 Graph of Drag Coefficient against Time for Simulation with PA Device Implemented on a Cube (1mN/m)

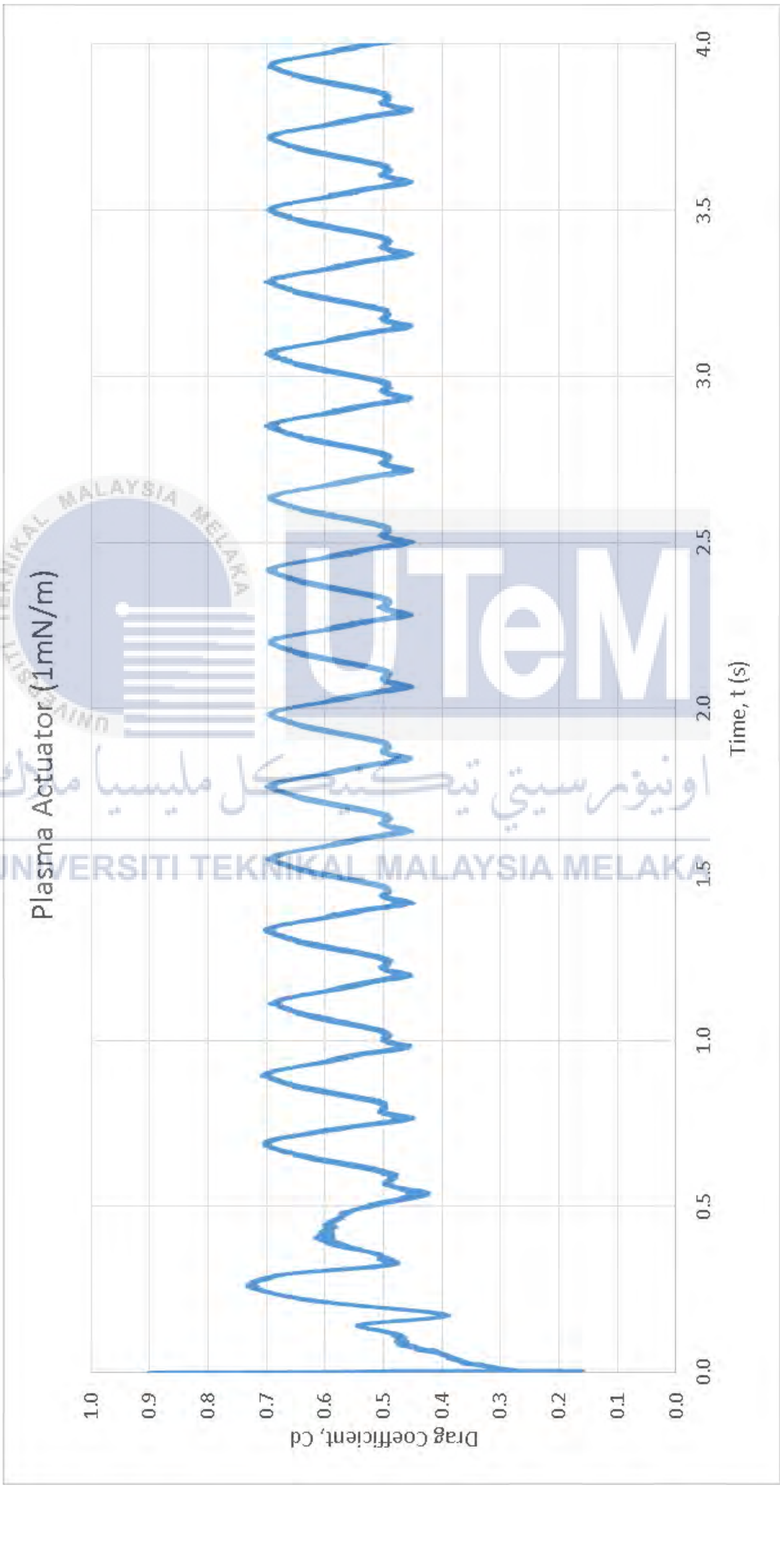

APPENDIX C2 Graph of Drag Coefficient against Time for Simulation with PA Device Implemented on a Cube (2mN/m)

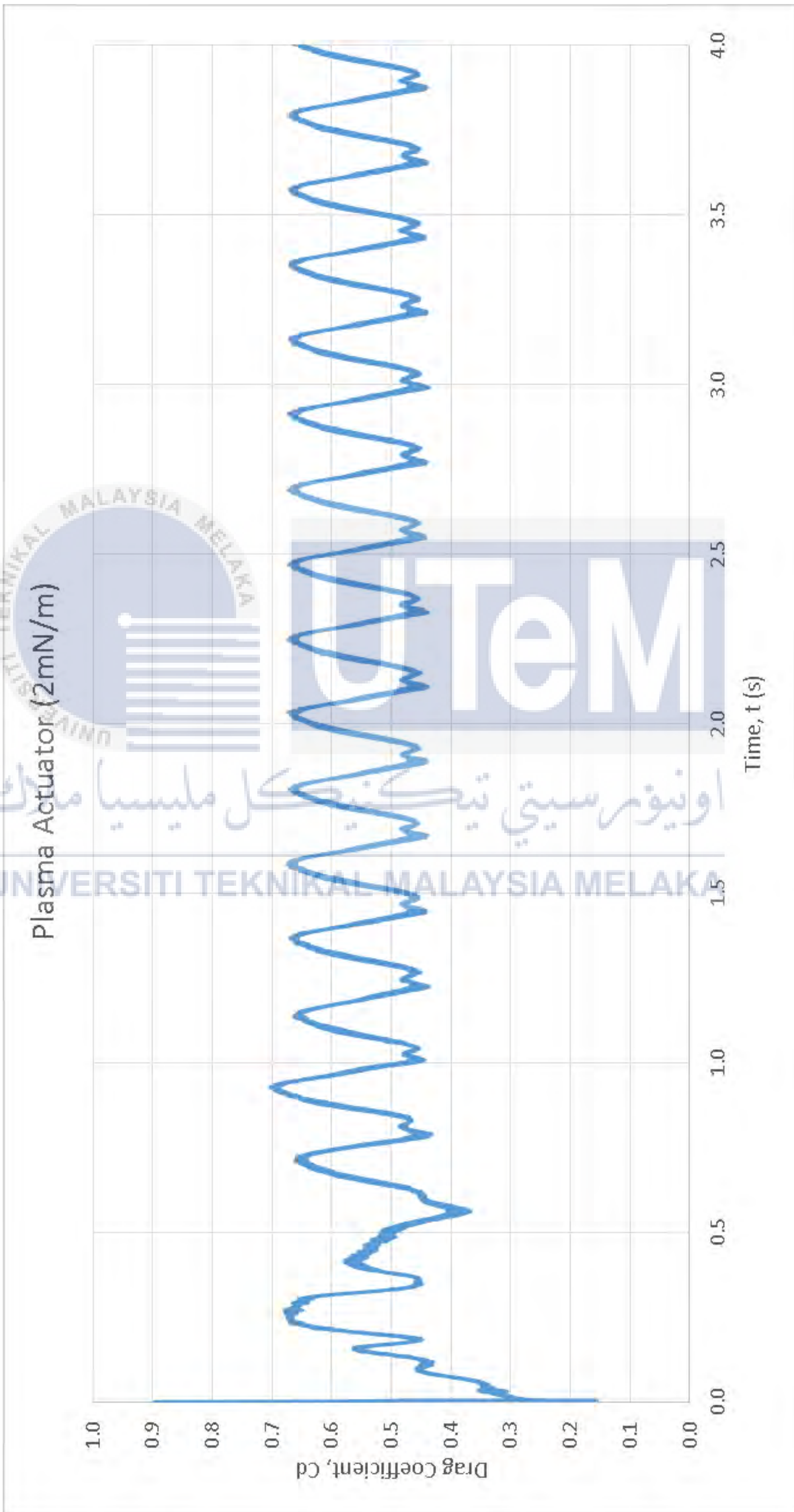

APPENDIX C3 Graph of Drag Coefficient against Time for Simulation with PA Device Implemented on a Cube (3mN/m)